Excitation of back-arc tsunamis from megathrust ruptures: Theory and application to the Sea of Japan

Amir Salaree[†‡] & Yihe Huang[*]

Department of Earth & Environmental Sciences
University of Michigan

[†] salaree@umich.edu
* yiheh@umich.edu
‡ *corresponding author*

1100 N University Ave., Department of Earth & Environmental Sciences,
University of Michigan, Ann Arbor, MI 48109

February 7, 2023

for submission to

Journal of Geophysical Research: Solid Earth

Abstract

Large megathrust ruptures can create notable tsunamis in tectonic back-arc basins as was documented during the 2011 Tohoku earthquake in the Sea of Japan. We present a physical analysis of the excitation of back-arc tsunamis by extending the fore-arc deformation field from the earthquake centroid into the back-arc basin and identify fault dip as the main geometrical contributor to the propagation of these events. As such, our theoretical model along with a large number of numerical simulations reveal that the dominant period of back-arc tsunamis is different from that of the fore-arc waves and thus they are a new class of tsunamis. Through numerical simulations and analysis of data from the 2011 Tohoku event, we show that a combination of near- to intermediate-field horizontal and vertical deformation as well as transient surface waves is necessary to reconstruct the back-arc propagation. We find that while seismic surface waves can affect coastal tsunami amplitudes in the back-arc, their effect comes second to that of the horizontal component of deformation as manifested via bathymetric gradient. We then simulate back-arc tsunamis and the hazard in the Sea of Japan from several potential future earthquake scenarios in the Japan Trench and Nankai Trough. Our results show that the coseismic excitation of back-arc tsunamis can result in considerable waves close to 1 m in the Sea of Japan, near the Niigata Prefecture from megathrust earthquakes.

Keywords: Tsunamis, Megathrust rupture, Back-arc basins, Sea of Japan, Surface waves

Plain Language Summary

The 2011 Japan earthquake created a large tsunami in the Pacific Ocean. But it also made a moderate tsunami in the Sea of Japan, on the far side of the Japanese islands. We call these waves *Back-arc* tsunamis and study their properties by looking at the contributions of various earthquake aspects including earthquake size, depth, fault geometry, and seismic surface waves, to the generation of these tsunamis. Our work shows that contrary to regular tsunamis, the hazard from back-arc tsunamis is affected by the fault dip angle (how steep the fault is). We also find that large earthquakes in eastern Japan can create relatively large back-arc tsunamis (with wave heights exceeding 1 m) in the Sea of Japan.

Key Points:

- We present theoretical and numerical models of back-arc tsunamis produced by megathrust earthquakes.
- Among source parameters, seismic moment and fault dip angles determine the dominant period and the spread of back-arc tsunamis.
- Back-arc tsunamis from Japan Trench rupture scenarios can reach amplitudes >1 m in the Sea of Japan, and should be included in hazard models.

1. Background and Motivation

Large megathrust earthquakes are often associated with tsunamis near the main deformation fronts at the fore-arc, e.g., 2004 Sumatra [e.g., Lay *et al*, 2005] and 2011 Tohoku [e.g., Mori *et al*, 2011]. However, secondary tsunamis have been reported in the tectonic back-arc basins during these same events by Grue *et al* [2008] and Murotani *et al* [2015]. In the case of the 2011 Japan event, the so-called back-arc tsunami was reported to reach an amplitude of ~50 cm and recorded by tide gauges around the Sea of Japan. Moderate waves were also reported by local fishermen at Niigata Prefecture [Murotani, *personal. comm.*].

The coseismic excitation of back-arc tsunamis is inherently different from the leakage of tsunamis into such basins from outside sources through narrow opening. The latter mechanism has been previously modeled by Shevchenko *et al* [2014] for the passage of the 2011 Tohoku tsunami into the Sea of Japan and the Sea of Okhotsk through the Tsugaru and Yuzhno-Kurilsk Straits, respectively (Fig. 1). However, this mechanism cannot explain the fact that the back-arc tsunami arrivals at the tide gauges in the Sea of Japan matched the origin time of coseismic rupture, not those of the fore-arc waves arriving much later. Murotani *et al* [2015] have instead concluded that such tsunami waves were excited coseismically and modeled the tsunami (perhaps the best documented event of this kind so far) using both vertical and horizontal components based on Okada's [1985] algorithm. In other studies of the complexity of the 2011 tsunami waveforms in Korea, Lee *et al* [2016] and Kim *et al* [2019] attributed the mismatch between synthetic and observed waveforms to the tsunami arriving from the north, i.e., the Sea of Japan (Fig. 1), concluding that the coseismic rupture of the Tohoku event excited the back-arc tsunami. We note that in Fig. 1, while generally it is expected that $T_3 > T_2 > T_1$, beaming the

simulated tsunami shows that the first and second rays have similar travel times ($T_1 \approx T_2$) as also documented by Kim *et al* [2019].

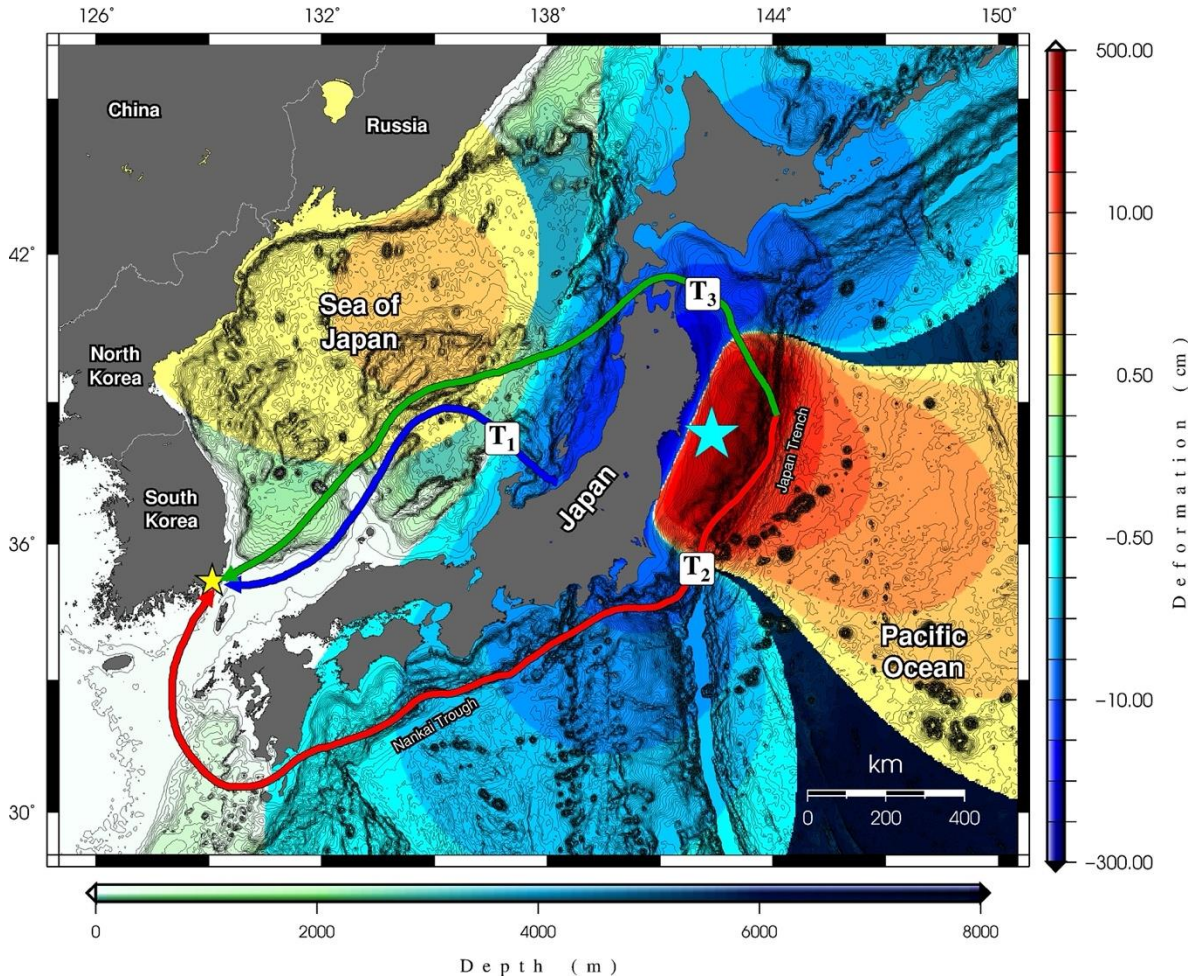

Figure 1. The three different approximate paths and their corresponding arrival times (T_i) for the 2011 tsunami to have reached Busan, Korea (yellow star) in the back-arc Sea of Japan. The colored background shows the offshore static, coseismic deformation field calculated from the CMT solution [Dziewonski *et al*, 1981; Ekström *et al*, 2012] of the mainshock. Black contours represent bathymetry [GEBCO, 2021]. Fault dimensions are calculated using earthquake scaling laws [Geller, 1976].

Nevertheless, the listed previous studies do not investigate the contribution of various source and basin factors to the frequency content of the back-arc tsunamis. While Murotani *et al* [2015] reported the poor mismatch in the high-frequency tsunami arrivals earlier in the

waveform, Kim *et al* [2019] applied a band-pass filter of 5 min to 6 hr to the tsunami waveforms and did not consider the high-frequency tsunami arrivals in their analysis. As a result, the behavior of back-arc tsunamis and their hazard at both high and low frequencies remain ambiguous.

The energy and hence the dominant period of fore-arc tsunamis is generally controlled by the ratio of water depth to source size [Okal, 2021], which for large earthquakes is traditionally considered proportional to the displaced volume of water, i.e., the hydrodynamic length scale of earthquake rupture [e.g., Plafker, 1997; Rabinovich, 1997; Okal & Synolakis, 2004]. Note that length scale is a dimension in hydrodynamic problems used to provide an expected order of magnitude for hydrodynamic velocity or dislocation features [Kundu et al., 2015]. The hazard associated with fore-arc tsunamis in the near-field is mainly a function of source geometry and dimensions [e.g., Okal & Synolakis, 2004; Satake *et al*, 2022] as well as coastal morphology [e.g., Salaree *et al*, 2021]. While coastal morphology is believed to be more significant on a local scale, the former has a more dominant effect throughout the propagation basin. Thus, the dominant frequency of the tsunami can be used as a first-order measure of tsunami hazard from a given source [Abe, 2006; Heidarzadeh & Satake, 2013].

The dominant frequency of fore-arc tsunamis has been shown to uniquely correspond to the fault width (the along-depth extent of faulting). In the absence of definitive constraints on the down-dip extent of ruptures in finite fault solutions (i.e., using both strong ground motion and teleseismic inversions) [e.g., Hartzell, S.H. & Heaton, 1983; Lay *et al*, 2010], scaling laws are often used to approximate fault dimensions [e.g., Geller, 1976; Scholz, 1982, Thingbaijam *et al*, 2017] and can provide estimates for fault width in the form of fractions of fault length, i.e., the along-strike dimension of rupture (e.g., in Fig. 1).

The dominant frequency of back-arc tsunamis, however, requires further scrutiny due to the absence of the main rupture front. Here, we first investigate the dominant frequency of back-arc tsunamis along with other source features through a physical dislocation model. We then use a large number of numerical simulations to identify the most important source parameters using synthetic as well as real data. In this regard, we consider the effects of both static initial dislocation and the transient surface waves from the mainshock. Motivated by the theoretical and numerical findings, we also evaluate the back-arc tsunami hazard in the Sea of Japan from various megathrust earthquake scenarios at the Japan Trench and the Nankai Trough. We show that considerable (~1 m) coastal amplitudes in the Sea of Japan are possible from such back-arc events.

2. Theory and Method

2.1 Deformation Model

Coseismic deformation caused by the strain release from large earthquakes usually spreads through wide areas (sometimes hundreds of kilometers) well beyond the subduction trench [e.g., Pollitz et al, 1996; Chlieh et al,, 2007; Pollitz et al, 2011]. The deformation in back-arc regions, however, is usually difficult to constrain using seismic and geodetic data and through finite fault models due the small slip amplitudes in deeper down dip areas. [e.g., Meng *et al*, 2011, Yokota *et al*, 2016]. The trade-off between depth, dip angle, and seismic moment in teleseismic inversions also hinders any definite resolution of slip at larger depths [e.g., Duputel *et al*, 2012].

Here we use the dislocation model from double-couple solutions to model the back-arc tsunamis (see the section 6). Such models are generally known as Okada solutions of the source and approximate static deformation from inclined buried faults in elastic half-spaces (Fig. 2). In contrast with finite fault models (see section S1 in supplementary material), the back-arc extension from these models is a continuation of the analytical expressions for the displacement fields of dip-slip faults. While the smooth deformation fields calculated from these models [e.g., Mansinha & Smylie, 1971; Okada, 1985] often do not consider bathymetry, the effect can be included in tsunami models by combining the horizontal component of deformation into the initial conditions for tsunami simulations [Tanioka & Satake, 1996]. The Okada solutions are routinely used in tsunami simulations due to their simplicity and robustness [Titov & Synolakis, 1998; Okal & Synolakis, 2004].

Fig. 2 is a simple cross-section of what we consider as the back-arc deformation model. The earthquake hypocenter and mechanism shown by a beachball is located on a fault plane depicted as an inclined, solid black line with a dip angle of δ, turning into an inclined dashed line to imply the uncertainty in the extent of down-dip rupture propagation. The deformed ocean floor (shown in orange in Fig. 2) displaces a body of water from static coseismic deformation in the back-arc (shown in red). It is the geographic span and volume of this amount of water that results in back-arc tsunamis, and consequently the source parameters contributing the most to back-arc tsunamis are those increasing this volume. We note that the robustness of Okada solutions in the back-arc from double-couple centroids overcomes their disadvantages such as the neglection of rupture kinematics, due to the shortcomings of other models in constraining the downdip slip at large depths.

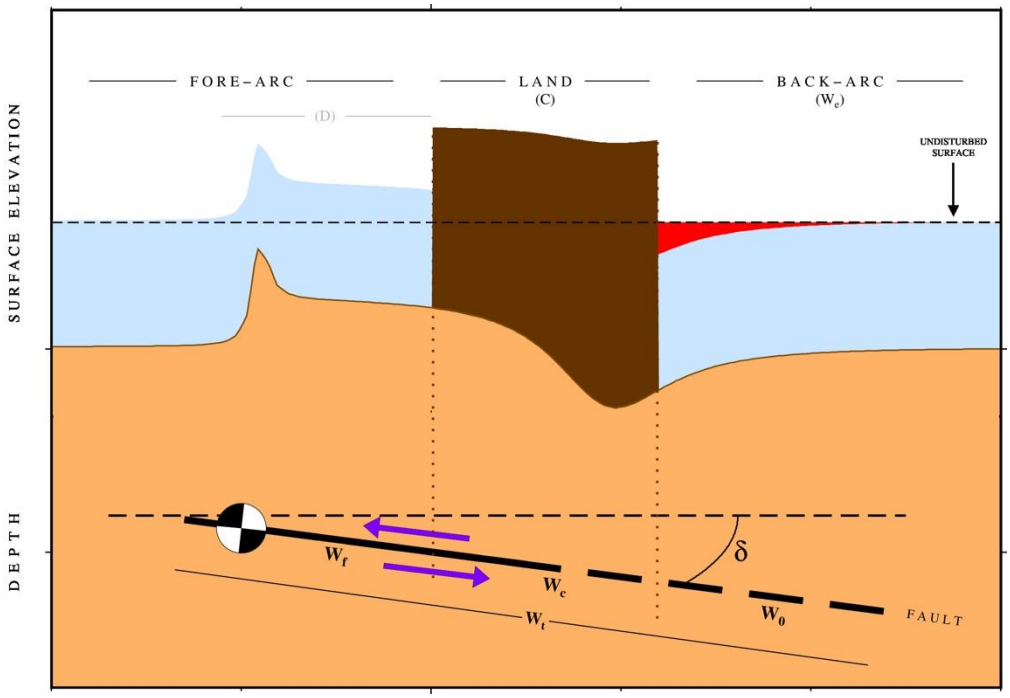

Figure 2. Along-dip cross-section of the dislocation model. Beachball represents rupture hypocenter. Purple arrows denote the down-dip fault motion. Ocean floor and water are shown in orange and blue, respectively. Back-arc displaced volume of water is depicted in red. δ represents fault dip. Definitions of length parameters are provided in section 3.

2.2 Tsunami Simulations

Using the calculated fields of static deformation (see section 2.1) as initial conditions, we apply the Method of Splitting Tsunamis (MOST) algorithm [Titov *et al*, 2016] to simulate the tsunamis and truncate the simulations at a shallow depth (10 m) close to the shorelines to avoid nonlinear features. MOST uses the fractional steps method originally developed by Yanenko [1971] to reduce the 2 + 1 problem of solving the 2-D differential shallow water version of Navier-Stokes equations into two simultaneous 1 + 1 problems [Titov & Synolakis, 1995; Salaree & Okal, 2015].

MOST has been extensively validated and applied in tsunami studies [Titov & Gonzalez, 1997; Synolakis *et al*, 2008; Tang *et al*, 2009]. Our simulations are carried out using a synthetic bathymetry grid with a resolution of 30 arc-seconds, and over 48-hr time windows with 1.5 s time steps to satisfy the CFL stability condition.

In each tsunami simulation, we record the tsunami time series at a virtual gauge in the geographic center of the back-arc basin. The dominant period is then numerically selected by carrying out a Fourier transform of the time series and picking the maxima of the amplitude spectra. In this process we avoid the very large resonance periods imposed by basin geometry through selecting an appropriate frequency range (T<6 hr). We note that such long-period oscillations are expected due to the closed or open nature of the back-arc basin as well as the long (48-hr) simulation window (section S2 in supplementary material). It should also be noted that non-geometric resonance, e.g., upon radiation at basin entrances [e.g., Berkhoff, 1976] and shelf overtones [e.g., Aranguiz *et al*, 2019] are not considered here.

3. Synthetic Experiments

3.1 Simulation Scenarios

To investigate the influence of source geometry (focal mechanism) and depth, we design deformation scenarios in a fore-arc—back-arc system as shown in Fig. 2. In these synthetic scenarios, a deep fore-arc (4000 m) is separated from a relatively shallow, closed and open (no boundaries to the north, south and east of back-arc), flat back-arc (1000 m) by a narrow (~50 km

wide) continent. The geometric setup is designed to accommodate the large width and breadth of real world back-arc basins, namely the Sea of Japan, the Caribbean, and the Gulf of Mexico where basin length scales exceed 15°. The closed basin was designed to test the effect of short-period basin resonance caused by internal successive reflections.

Megathrust events tend to occur in shallow depths (<40 km) with the majority of accumulated strain released within the crust and close to the trench. Based on our dislocation model (Fig. 2), earthquakes with larger seismic moment (i.e., larger ruptures) or those closer to the continental arc are naturally expected to create larger back-arc tsunamis as they would displace more water on the opposite side of the continent. However, as large (M>8.0), shallow megathrusts capable of generating large back-arc tsunamis tend to occur at or in the vicinity of trenches, the most loosely constrained source parameter will be the source geometry instead of location. Although as a global average, trenches are located ~250 km away from continents, depending on the shape, size, and physical properties of the megathrust zone, these ruptures can take place only slightly closer to land [Bilek & Lay, 2018]. Therefore, the magnitudes of megathrusts also determine the extent of down-dip faulting and thus that of back-arc deformation (see Fig. 2).

While larger dip angle of source ruptures would result in more significant vertical components of initial deformation, and thus larger tsunamis at least in the near-field as shown in Fig. 3 [e.g., Titov *et al*, 1999; Gica *et al*, 2007], megathrusts tend to occur at shallow dips (δ<30 ^{o}) and with slip vectors almost perpendicular to the trench ($45^{o} < \lambda < 135^{o}$). In fact, the global median of dip angles for M_w>8 events from the CMT catalog is $\delta \approx 19^{o}$ (the vertical dashed line in Fig. 3).

One can show that meaningful back-arc deformations in this setup would only occur for megathrust events and thus we set a $M_0=1.3\times10^{28}$ dyn-cm ($M_w=8.0$) as the minimum seismic moment in our designed scenarios. We also set $M_0=2.2\times10^{30}$ dyn-cm ($M_w=9.5$) as the high end of rupture moments. The latter moment may be excessive but is chosen to accommodate the worst-case scenario (as was the case during the 20 May 1960 M9.5 Chilean rupture).

By taking these geometric constraints into account, we design a large number of synthetic scenarios by placing source centroids in the fore-arc, 75 km away from the continent at a central latitude (representative of arc systems with narrow continents and high potential of back-arc tsunamis, e.g., Oaxaca). Each scenario is designed as a set of (M_w, H, δ, λ) (i.e., magnitude, centroid depth, dip, and slip) with $8.0 \leqslant M_w \leqslant 9.5$, 10 km $\leqslant$ H $\leqslant$ 40 km, $10^o \leqslant \delta \leqslant 40^o$, and $40^o \leqslant \lambda \leqslant 90^o$ (benefiting from the axial symmetry along latitude) while keeping the rupture strike the same as that of the trench, assumed to be parallel to the continental arc (see Table S1 in the supplementary material). The choice of depth range is valid due to the nature of centroids and has been documented for large megathrust events in the past (e.g., the 2011 Japan [Ide *et al*, 2011]). We then calculate static deformation fields based on the algorithm by Mansinha & Smylie [1971] as a type of Okada algorithms using earthquake scaling laws for uniform slip (Geller, 1976; $M_0= 1.45\times10^{20}.\Delta\sigma.L^3$ with $\Delta\sigma$ and L as a constant stress drop and fault length where the fault length is related to its width W by L=*x*W where *x* depends on earthquake magnitude, etc). Under scaling laws, earthquake dislocation (regardless of source parameters, e.g., focal geometry, depth, etc) are invariant of stress drop, and assuming constant rigidity, of strain release [Okal & Synolakis, 2004]. The scaling leads to approximations for fault dimensions and slip which have been extensively benchmarked using large datasets of earthquakes and tsunamis [e.g., Thingbaijam *et al*, 2017]. In these simulations, by choosing

centroid over hypocenter, we have ensured that the ruptures do not breach free surface, hence abiding by the requirements of Okada algorithms. Besides, by confining the fault width within the global depth of the seismogenic zone for megathrusts, i.e. 40 km, we have avoided unrealistic faulting.

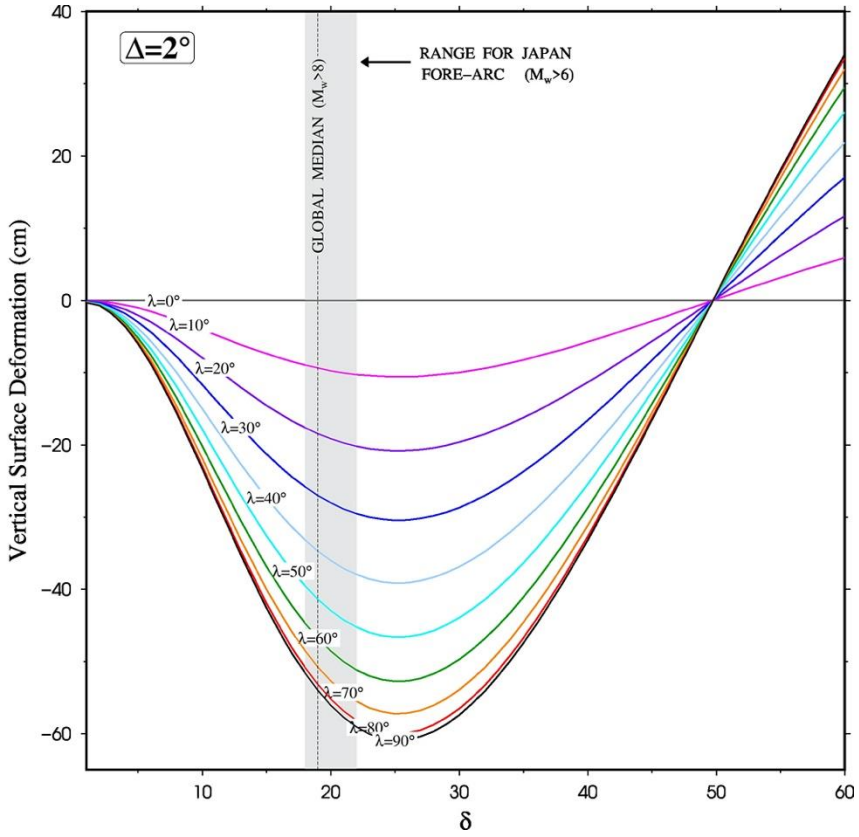

Figure 3. Calculated vertical surface deformation at a distance of Δ=2º from the hypocenter as a function of fault dip (δ) for various slip angles (no fore-arc/back-arc systems are imposed). Calculations are carried out for a M_w=9 source with a 5-km deep centroid; slip is scaled to seismic moment using Geller [1976]. The vertical dashed line and the hatched area represent the global median (M_w>8) and the range of dip angles for the Japanese events, respectively, from the CMT catalog.

3.2 Simulations

We use these scenarios to simulate back-arc tsunamis using the strategy described in sections 2.2 and 3.1. Examples of these scenarios and their simulation results are shown in Fig. 4. The left panels in Fig. 4 (Figs. 4a & 4b) show the initial deformation fields calculated for M_w=9.0 scenarios with constant depth and slip angle (λ=90º) and at two different dip angles ($\delta = 10°$ and $\delta = 20°$). The middle panels (Figs. 4a' & 4b') show the simulated maximum tsunami amplitudes from the two scenarios in Figs. 4a & 4b. The spectra for the simulated tsunamis in closed and open back-arc basins are shown in Figs. 4a" & 4b" as blue and red curves, respectively. Dominant periods from simulations are depicted by red, dashed lines.

Similar comparisons can be drawn for other designed scenarios with different parameters (i.e., seismic moment, focal depth, and slip angle) as shown in Fig. 5. The double-primed panels in Fig. 5 show the spectra of the time series from virtual gauges (yellow stars) in each corresponding scenario shown on the left. The blue and red curves in these panels belong to simulations in closed and open (back-arc basin is not bounded) back-arc basins. We can see in Fig. 5 that the spectral contents of the closed and open cases in each scenario are very similar with the closed cases behaving as a discretized version of the open counterparts. Meanwhile, the similar dominant periods across the two suggest that basin properties come second to earthquake source properties in affecting the back-arc tsunami spectra. We note that the virtual tide gauge used in the spectral analysis is placed at the geographic center of the basin (yellow stars in Figs. 4 and 5), far from the boundaries and significant, static deformations (from source) and is thus a good measure of the tsunami propagation. We attribute the beating spectral nature of the tsunami in closed back-arc basins to the oscillatory modes from multiple reflections of hydrodynamic standing waves. Due to the spectral similarity of closed and open cases in each scenario, as well

as the smoother nature of the spectra in the open case, we will focus on the latter as the representative for back-arc tsunamis in the rest of the paper.

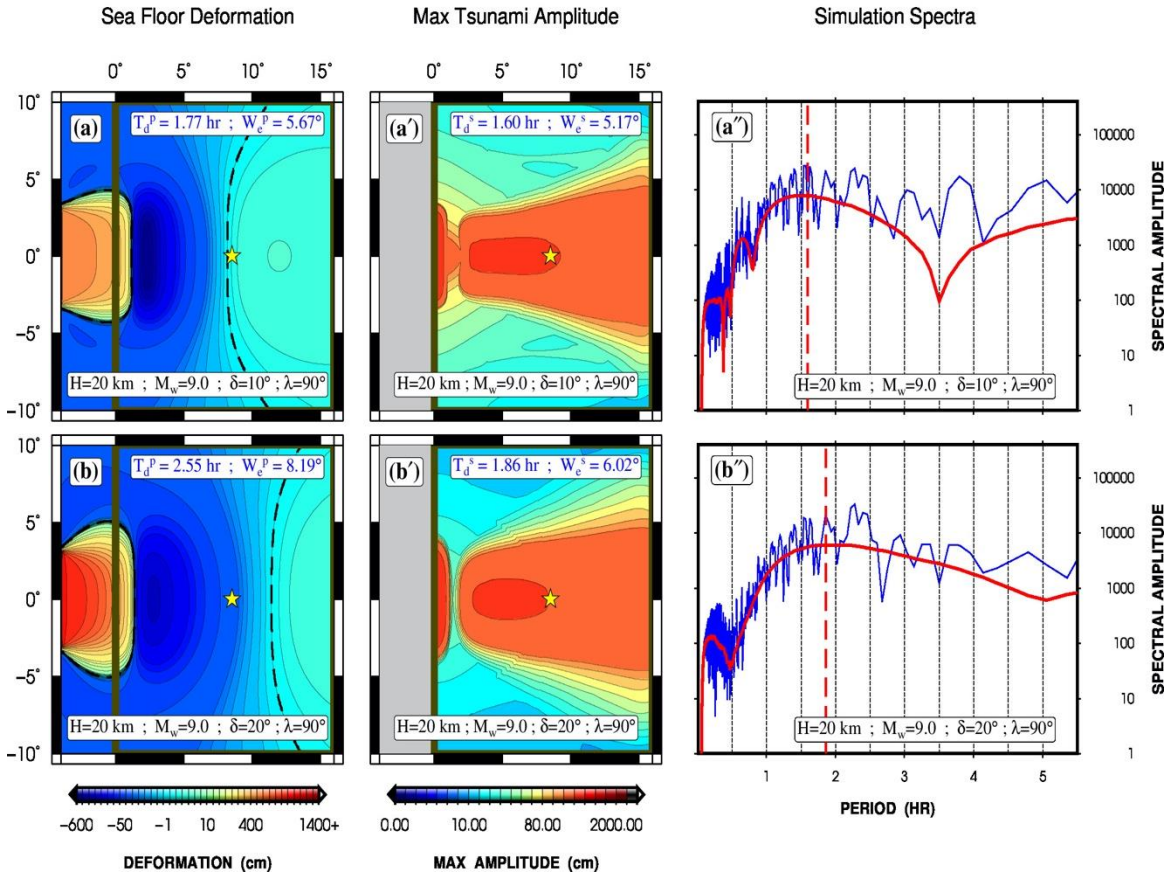

Figure 4. (a),(b) Ocean floor deformation fields calculated from M_w 9.0 point sources in the fore-arc for two dip angles (10º and 20º). Black, dashed lines show the deformation nodes (i.e., zero deformation). In each panel, dominant tsunami periods from numerical simulations (T_d) and the corresponding length scale (W_e) to those periods are listed. The 'p' and 's' superscripts denote values predicted from our model, and those from hydrodynamic simulations, respectively (see sections 3.1 and 3.2). **(a'),(b')** Simulated maximum tsunami amplitudes from the scenarios in (a) and (b). Fore-arc values are masked in gray to focus on the back-arc tsunami. **(a"),(b")** Spectra of the simulated tsunamis at virtual gauges (yellow stars) in each corresponding scenario in (a) and (b). The blue and red curves are from scenarios with closed and open back-arc basins, respectively. Red, dashed lines show spectral maxima of the red curves. Time series for the virtual gauges are shown in Fig.

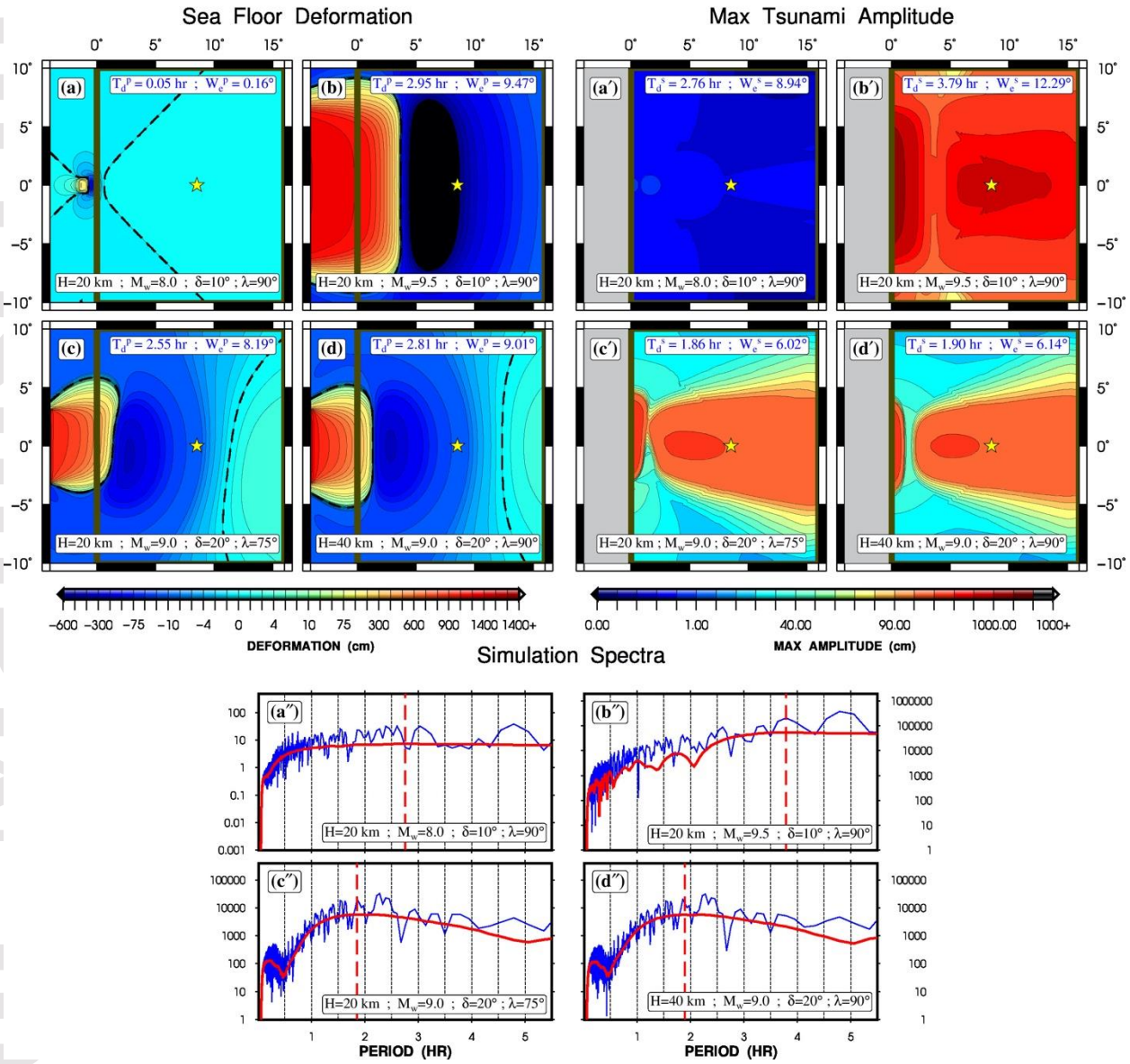

Figure 5. Similar to Fig. 4, but for scenarios with different geometries and sizes. Note the different vertical scales across (a") to (d").

It is readily seen in our simulation results (Figs. 4 & 5; also see Table S1 in supplementary material) that similar to the far-field manifestation of their shallow, fore-arc counterparts [e.g., Ward, 1980], the effect of centroid depth on back-arc tsunamis is not significant (e.g., note the differences between Figs. 4b and 5d as well as their primed and double-primed counterparts). In comparison with the effect of varying depth, changing the slip angle (λ) leads to a more significant change in the back-arc propagation pattern, and the metric MT as a measure of difference between tsunami propagation maps has a value three times larger between Figs. 4b' and Fig. 5c' than that between Figs. 5c' and Fig. 5d' ($MT=9.8\times10^{-6}$ compared to $MT=2.9\times10^{-6}$). Among all the source parameters tested in the dislocation models, variations in dip angle (δ) cause the largest changes in the back-arc tsunami, e.g., $MT=1.1\times10^{-5}$ between Figs. 4a' and 4b'. We recall that MT is a pointwise comparison metric for two congruent tsunami propagation maps, and that smaller values of MT correspond to more similar propagation fields [Salaree & Okal, 2020].

Our simulations of back-arc tsunamis in these synthetic scenarios show larger tsunami amplitudes at higher dip angles, similar to their fore-arc counterparts (Fig. 6). This is due to the increase in the deformation amplitude at higher dip angles ($\delta \leqslant 45^{o}$) (Fig. 3). We attribute the decrease in maximum tsunami amplitudes at higher dip angles for smaller sources (M_w=8.0 and 8.5) in Fig. 6 to the transition of significant deformation values from the back-arc basin under the continental arc. This results in the exclusion of the corresponding initial conditions from tsunami simulations.

Our results also show that contrary to fore-arc tsunamis, the back-arc dominant period is not constant, i.e., not uniquely determined by fault width [Rabinovich, 1997]. In Figs. 5a'' to 5d'',

dominant periods are picked as the maxima of the computed spectra (shown by vertical, red, dashed lines). We note that, as expected, seismic moment is the main factor affecting the dominant period of back-arc tsunami (e.g., see Fig. 5b" and Table S1), but we find the dominant period also varies with the dip angle of the fault plane.

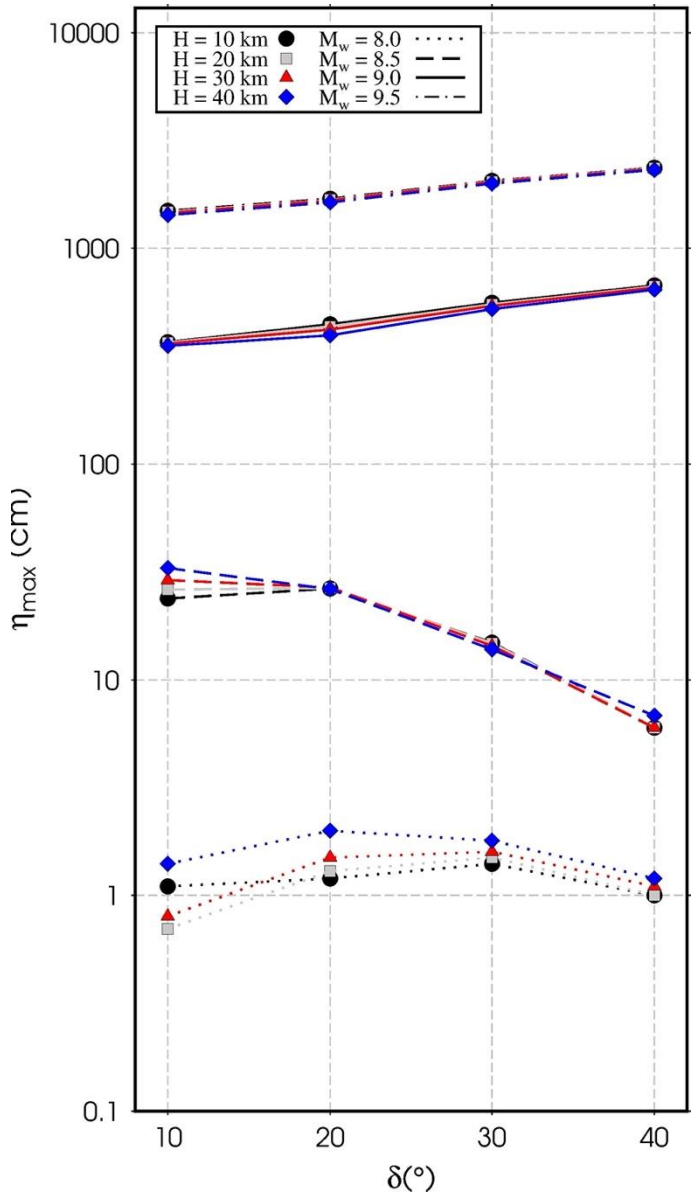

Figure 6. Variations in maximum back-arc tsunami amplitude, η_{max}, as a function of dip angle (δ), centroid depth (H) and moment magnitude. Colors and patterns of each curve represent different depths and magnitudes.

3.3 Dipping Plane Model

Our observations can be explained by studying how seismic moment and dip angle of the rupture would affect the extent of back-arc deformation. In the absence of the main, fore-arc rupture front, one can model the horizontal extent of negative polarity surface deformation in the back-arc as the projection of the fault plane on the far side of the continental arc onto the surface (Fig. 7). In this formalism, seismic moment, and thus the along-dip length of the fault plane is the main factor affecting the horizontal length scale or *effective width*, W_e, of surface deformation. Also, dip angle (δ) affects W_e upon projecting the actual fault width, W_0, to the surface in the form of $W_0 \cos\delta$. Determining the back-arc source depth is a more complex issue in this model as it is expressed in the form of a secondary depth, i.e., H_e in Fig. 7, which is related to the centroid depth, H_0, as $H_0 + W_0 \sin\delta$ where δ is the dip angle. From the tsunami point of view, in the absence of a fixed point as hypocenter or centroid in the back-arc, this quantity is not constant and varies along the downdip plane.

We note that the total fault width (W_t) as inferred from teleseismic data is the sum of fore-arc, subcontinent, and back-arc along-dip segments of the fault plane as depicted in Fig. 2 by W_f, W_c, and W_0, respectively:

$$W_t = W_f + W_c + W_0 \quad (1)$$

or,

$$W_t = \frac{1}{\cos\delta}(C + D + W_e) \quad (2)$$

where *C* represents the width of continental arc, and *D* is the trench-to-continent distance (see Fig. 2).

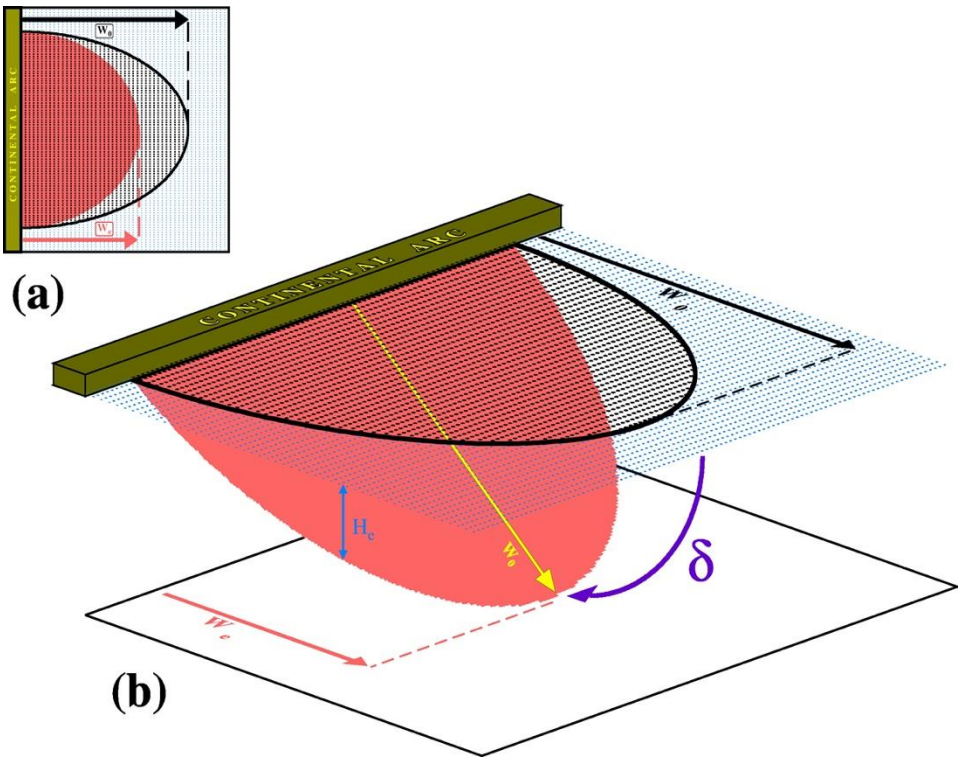

Figure 7. (a) Map view and **(b)** side view of the surface projection of rupture plane onto the surface. H_e, W_0 and W_e are the contribution of rupture in the back-arc (i.e., effective depth) to apparent depth, width of rupture plane in the back-arc, and effective width of the rupture. δ represents fault dip.

We can use this model to predict the dominant period of back-arc tsunamis, by measuring the largest distance between successive maxima and minima in the zero-latitude cross-section of back-arc deformation, as shown in Fig. 8 which is equivalent to the effective width in our model. We note that Fig. 8 shows narrow sections at zero latitude in the deformation

fields and thus the lack of symmetry in the non-pure mechanisms (λ≠90°) does not impose an issue to our simple model. For each source scenario (e.g., the panels in Fig. 8) we can compute a corresponding dominant period using the measured effective width (W_e) and the group velocity of tsunami from shallow water approximation ($c = \sqrt{gh}$). The latter is valid due to the large length scale of the back-arc source and the shallow (1000 m) flat ocean (for effects of slip angle, see section S3 supplementary material).

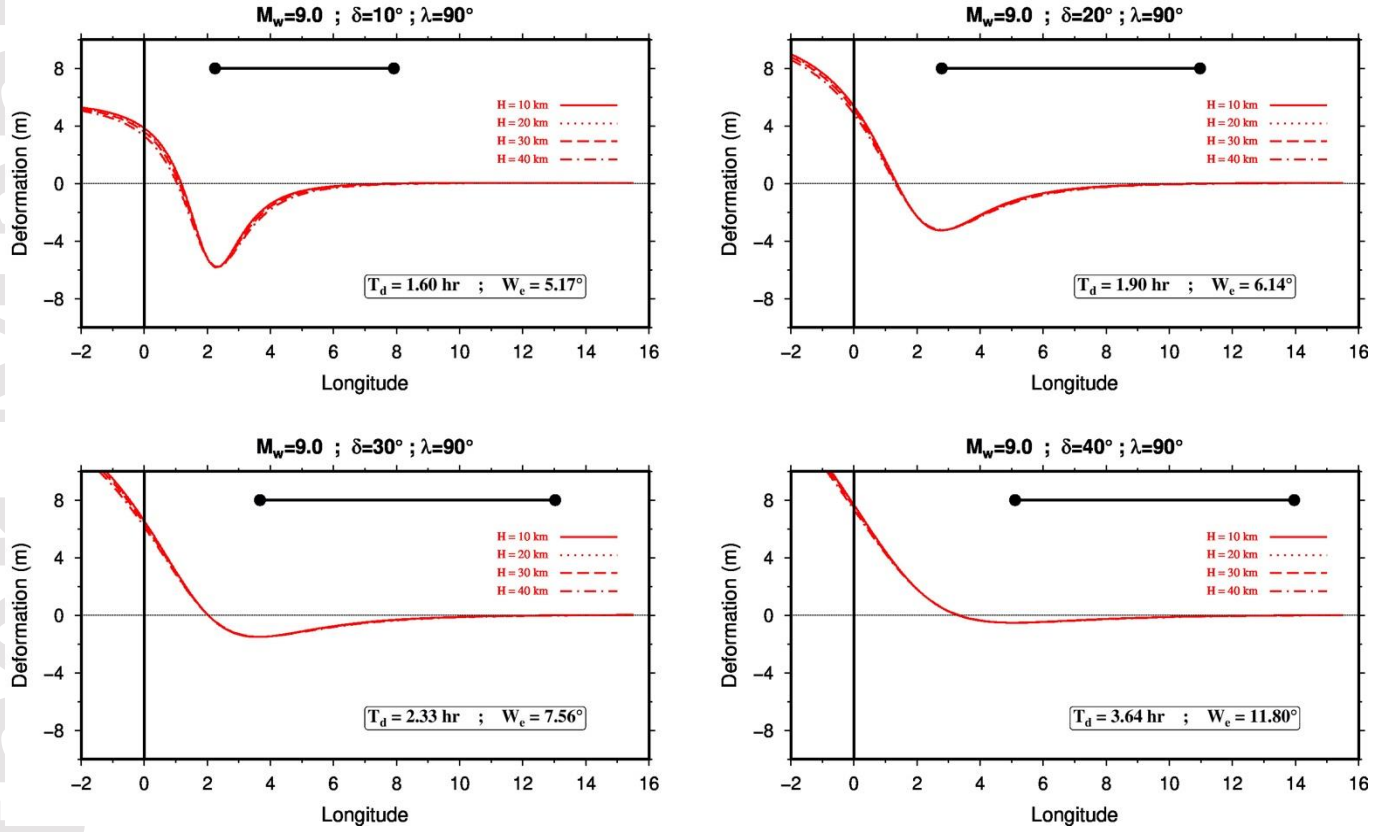

Figure 8. Measuring effective widths (black, horizontal lines) at various dip angles as the largest distance between successive maxima and minima in the cross-section of back-arc deformation. The panels show cross sections from four scenarios with different dip angles at λ=90º. Red curves in each panel represent scenarios with various centroid depths. Dominant periods, T_d, are calculated from their corresponding effective widths, W_e.

This model predicts larger dominant periods for the back-arc tsunamis at larger dip angles (see section 6 for the discussion of mismatch), in agreement with the results from our hydrodynamic simulations, as shown in Fig. 9. The effective width in this simple model explains the quadratic fits to the calculated dominant periods at various dip angles in Fig. 9 as they can be thought of Taylor expansions with small quadratic coefficients of the cosine function (Eq. (2)). It is noteworthy that Eq. (2) provides a proxy to constraint the down-dip extent of rupture upon measuring the dominant period of back-arc tsunami, and hence estimating the total width.

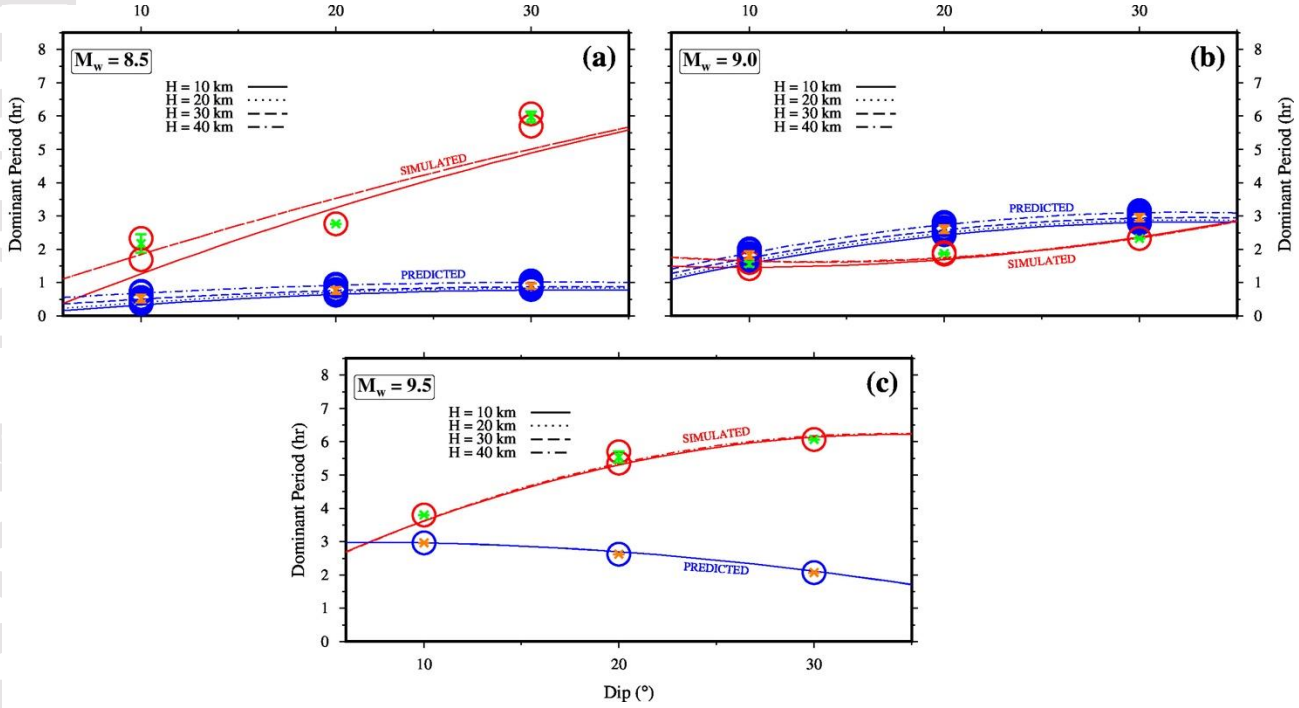

Figure 9. Variations in back-arc dominant period as a function of changes in dip angle from four source scenarios with different magnitudes. In each panel, blue and red circles represent respectively predicted and simulated dominant periods for various centroid depths. Orange and green vertical lines are error bars at each dip angle for the predicted and simulated groups, respectively. The shown curves are quadratic fits to each depth scenario.

As shown in Figs. 4, 5, and 9, our model provides a reasonable estimate of the back-arc spectral maxima across various dip angles for the M_w=9.0 scenarios. We attribute the disagreement between the predicted and simulated dominant periods of back-arc tsunamis for M_w=8.5 and M_w=9.5 (scenarios compared to the M_w=9.0) to the deviation of deformation fields from our proposed model. In the M_w=8.5 scenarios, a considerable part of negative polarity deformation is located in the fore-arc (as W_f and W_c) and hence does not contribute to the back-arc tsunami. At the other end, vast positive deformation parts of the significantly larger M_w=9.5 source leak into the back-arc, thus violating our assumption of negative-only deformation in our simple model (see Figs. 2, 5b and 7). In other words, in M_w=8.5 and M_w=9.5 scenarios, we are respectively undersampling and oversampling the back-arc source deformation. We note that the positioning of our source scenarios is constrained by physical and tectonic properties of the back-arc basin and location of trench. This inevitably results in deviations of simulation scenarios from our simple theoretical model. Fig. 10 demonstrates how the width of continental arc can affect the working threshold of our model. In Fig. 10, various widths of the continental arc result in different polarities of deformation to be exposed or hidden from the back-arc basin. For instance, while in a 50 km wide arc (i.e., our simulations) an M_w=8.7 source is the ideal scenario for our model, for an M_w=8.9 event a 200 km wide arc in our model works best. Finally, we attribute the under- vs. overestimation of back-arc amplitude by our model to the nonuniform trigonometric projection of fault plane to the surface, as well as the expressions of the nonlinearity in the Navier-Stokes equations which is missing from our models.

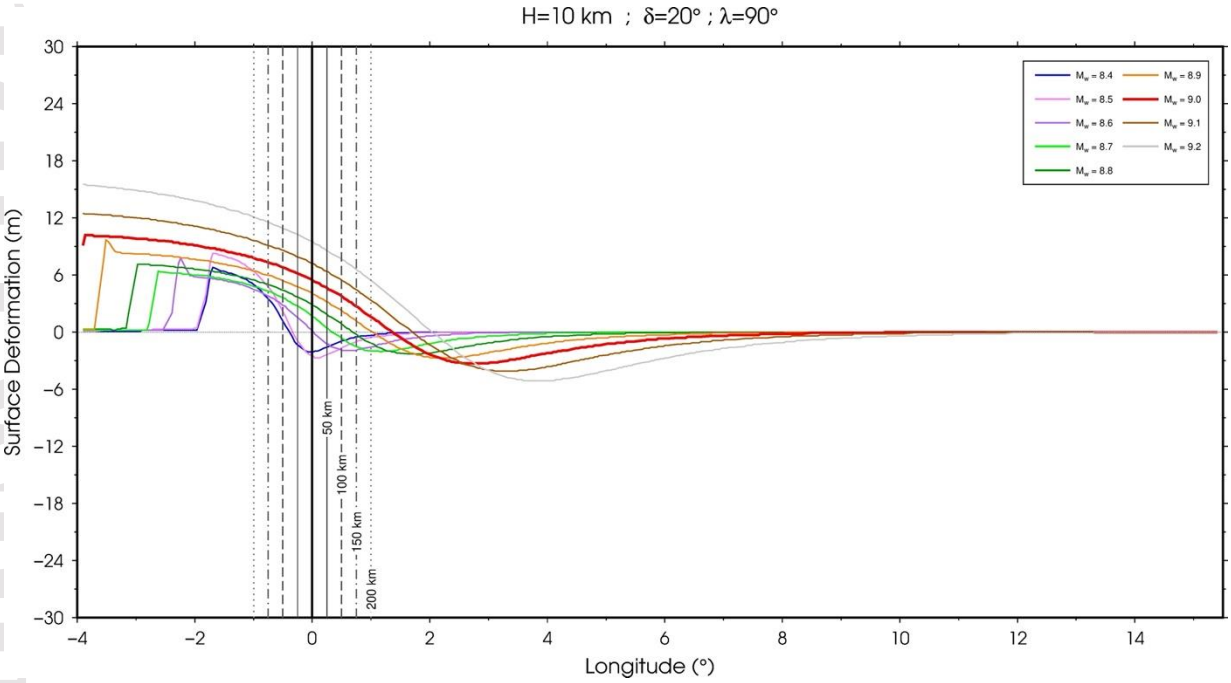

Figure 10. Deformation profiles from $8.4 \leq M_w \leq 9.2$ earthquakes (at 0.1 magnitude increments) throughout the fore- and back-arc domains. The vertical lines depict continental arcs with various total widths, labeled in km.

These results show that the back-arc tsunami hazard is dominated by earthquake magnitude and the dip angle of the fault plane. In fact, our simulations show that a magnitude 9.0 earthquake can result in back-arc tsunamis reaching ~1 m amplitudes (Fig. 6). At the same time, larger tsunamis are expected for sources with larger dip angles, and that these tsunamis have a lower frequency content (red-shifted) resulting in less energetic tsunamis. We note that while we have carried out our simulations in ideal, flat back-arc basins, the presence of complex bathymetric features would complicate the propagation of these tsunamis. Also, the abundance of concave coastal morphology in the far side of continental arcs is expected to increase the back-arc coastal tsunami amplitudes. With these points in mind, we proceed to investigate the back-arc tsunami hazard in the Sea of Japan where there has been a well-documented example of back-arc tsunamis in the past.

4. Back-arc Tsunamis in the Sea of Japan

Here, we use our findings from sections 2 and 3 to obtain a better understanding of back-arc tsunamis in the Sea of Japan. The Japan Trench has hosted the 2011 M_w=9.0 Tohoku rupture, one of the largest recorded earthquakes in the instrumental era. At the eastern margin of the Japanese Islands, the convergence between Pacific and Okhotsk plates has resulted in an active subduction which has experienced numerous megathrust earthquakes and therefore tsunamis in the past [e.g., Hashimoto *et al*, 2009; Satake, 2015]. Similarly, in the south, the subduction of Philippines plate under the Eurasian plate has generated a rich history of large earthquakes along the Nankai Trough [e.g., Ando, 1975; Ishibashi, 2004; Yokota *et al*, 2016].

Both the aforementioned subductions have created M9 earthquakes and larger in the past and are expected to do so in the future. Therefore, the excitation of back-arc tsunamis from any such event needs to be considered while studying the tsunami hazard in the Sea of Japan.

4.1 The 2011 Tohoku Earthquake and Tsunami

The 2011 M_w=9.0 Tohoku earthquake created perhaps the best recorded back-arc tsunami to this date, mainly due to the dense population of tide gauges all around the Sea of Japan. This earthquake ruptured a ~200 km × ~400 km patch of the Pacific-Okhotsk plate boundary along the Japan Trench [Ammon *et al*, 2011; Ide *et al*, 2011; Shao *et al*, 2011; Lay, 2018] with unusually large slip, up to 50–80 m [Fujiwara et al, 2011; Ito *et al*, 2011a]. The shallow CMT

hypocenter at ~25 km combined with the large slip resulted in large values of ocean floor uplifts of near the coastline, as well as ~30 m vertical and ~60 m horizontal displacements at the trench, respectively [Kido *et al*, 2011, Ito *et al*, 2011b]. The large areas of uplift and subsidence at the ocean floor [Grapenthin & Freymueller, 2011] generated a devastating tsunami reaching 40 m along the Sanriku coast [Mori *et al*, 2011; Shimozono *et al*, 2012].

However, the coseismic deformation was not limited to the trench side of the Japan island – the fore-arc. In fact, geodetic measurements documented decimetric and centimetric deformations in the western Japanese coastlines [Pollitz *et al*, 2011]. This so-called back-arc field of deformation would continue into the Sea of Japan and result in a complex pattern of uplift and subsidence at the sea floor. Numerical models also successfully predict centimetric deformation westward across the Sea of Japan reaching Russia [Pollitz *et al*, 2011; Sato *et al*, 2011]. Such back-arc deformations are expected from our models based on the Okada solutions (Figs. 1 and 2). The resulting moderate back-arc tsunami was recorded by tide gauges all around the Sea of Japan including in Japan, Korea and Russia.

4.2 Tide Gauge Data

To investigate the propagation of the 2011 back-arc tsunami, we use data from three tide gauges along the western coastlines in Rudnaya Pristan, Preobrazheniye (both in Russia), and Busan (Korea), as well as five tide gauges from Geospatial Information Authority of Japan (GSI) on the Japanese coast (Fig. 11a). These stations provide a reasonable azimuthal coverage of the tsunami around the Sea of Japan. The Busan station is used to analyze the critical interaction of

fore- and back-arc arrivals. The time series from the Russian and Korean sites are sampled at 1-minute, and and Japanese data are sampled at 30-second intervals. The data is de-tided by applying a 6-hr filter which (as discussed in section 2) also helps with removing the effects of basin-wide resonance.

4.3 Contribution of Surface Waves

Upon modeling the 2011 back-arc tsunami, Murotani *et al* [2015] expressed concern regarding the match between tide gauge data and their simulations at high-frequencies. To investigate this issue, we also include the contribution of seismic surface waves to tsunamis which can affect the higher end of the frequency content of tsunamis due to their high amplitudes and wide spectral range [Barberopoulou et al, 2004; Saito *et al*, 2019]. Our simulations consider the initial deformation from Rayleigh waves which typically possess higher frequency content than the longer period tsunami waves. Using a normal modes approach, we calculate surface wave eigenfunctions down to ~150 seconds (see section S4 in supplementary material). This corresponds to a spatial resolution of ~30 km in the Sea of Japan, which is shallower than 4000 m, and should be sufficient considering the large source dimensions.

4.3 Simulation of Tsunamis in the Sea of Japan

We carry out tsunami simulations in the GEBCO bathymetric grid with a spatial resolution of 30 arc-seconds [Weatherall *et al*, 2015] using (a) vertical deformation, (b) both vertical and horizontal deformations for the CMT solution, and (c) a combination of surface

deformation and Rayleigh waves (more details are shown in supplementary material). Simulations cover the geographic window of 124°-150°E and 28°-46°N and a 48 hr time window after the rupture origin time and use 1.5 s time steps to satisfy the CFL condition. While our virtual gauges are often placed at a distance of several kilometers from shorelines, we terminate the computations at the depth of 10 m to avoid nonlinear effects including those caused by harbor resonance (similar to the strategy in section 2.2).

Fig. 11a shows the simulation result from the superposition of all three deformation sources as initial conditions. Each panel in Fig. 11(b–d) shows the simulated time series compared to recorded data (black curves) as well as their correlation coefficients (CC) for 30-minute time intervals (see sections S5 and S6 of the supplementary material for the longer time series). Variations in the calculation intervals for CC shows that 30 minutes is an approximate threshold after which the rate of change in CC as a function of calculation interval decreases. The choice of CC over amplitude matching is due to the fact that CC is a better representation of variations in signal's trend (i.e., period). Also, the large-scale apparent amplitude mismatch (Fig. 11) is likely caused by our simple uniform-slip source model which does not incorporate the variations in down-dip moment release [Kanamori *et al*, 2019].

Similar to this study, Murotani *et al* [2015] were more successful in matching the observed signals from stations at the far side of the Sea of Japan. The discrepancy near the coast of Japan is possibly due to the effect of bathymetry caused by the horizontal component of deformation. We attribute the practically non-existing coseismic amplitudes and the signal complexity in Busan (similar issues can be seen at Okushiri in the north) to its proximity to the deformation node (Fig. 11a). Beamforming of tsunami waves in the Korea Strait shows that the slower back-arc waves (from the shallow continental shelf) arrive at Busan only slightly earlier

than the faster fore-arc waves (from the deep trench). The flip-flops in the dominant azimuth of arriving tsunami waves near Busan shows significant changes in the propagation direction as well as the influence of large-scale reflections (section S7 in supplementary material). Thus, the first arrival is an emergent phase with negative polarity (edge waves from the nearby coseismic coastal depression in the back-arc). Later on, this signal mixes with the positive polarity, fore-arc signal in a complex pattern, hence resulting in the poor fit of the simulations. This underlines the importance of source geometry in excitation of back-arc tsunamis.

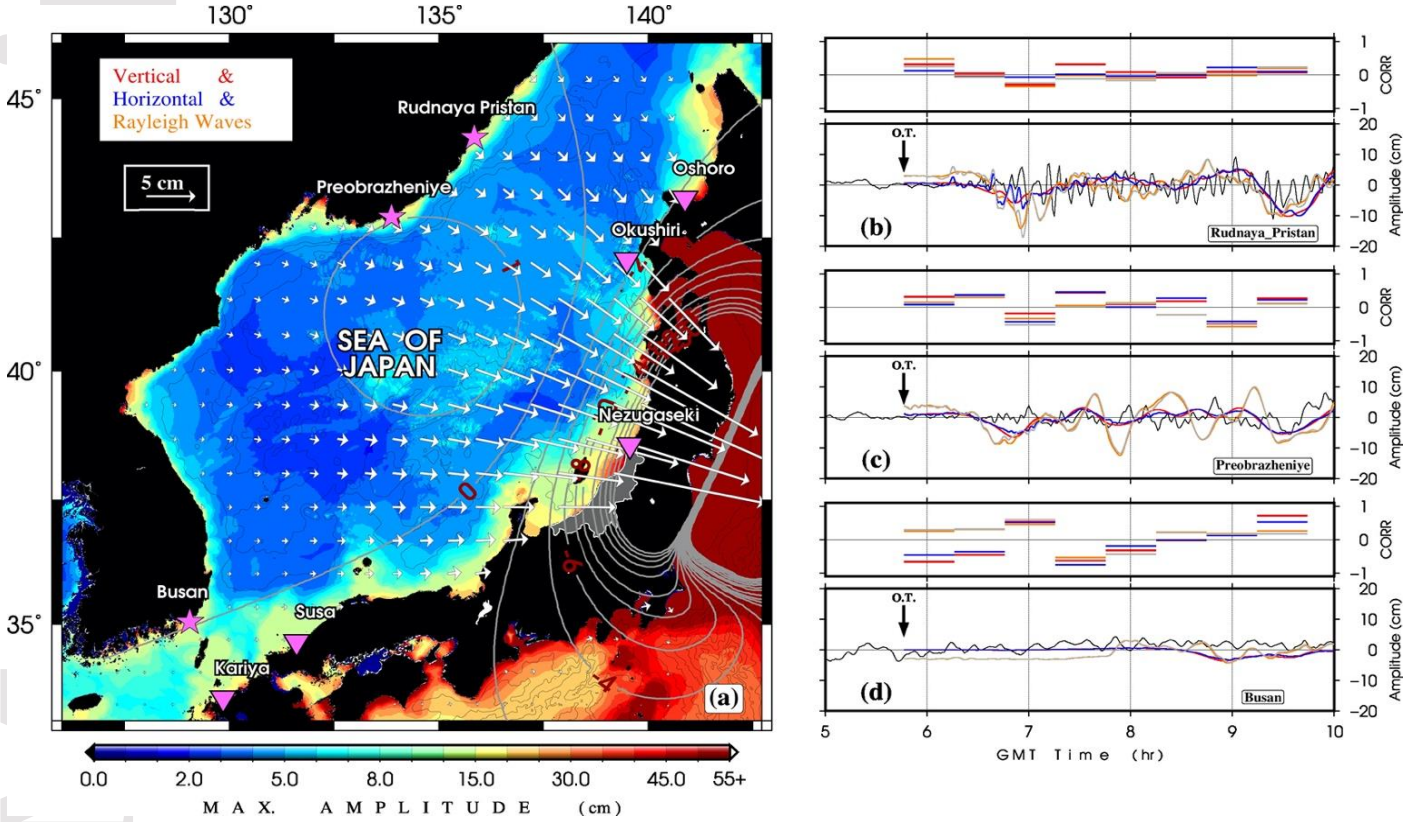

Figure 11. (a) Simulation of the tsunami in the Sea of Japan from the 2011 Tohoku earthquake using both vertical and horizontal components of static deformation from the CMT source as well as the Rayleigh waves. Gray contours represent the vertical static deformation, labeled in centimeters. Arrows are scaled to the horizontal component of deformation field. The Niigata Prefecture (the location of largest reported waves) is shown as a shaded part of western Japan. **(b—d)** Tide gauge records from the 2011 Japan tsunami at three locations: (b) Rudnaya Pristan, (c) Preobrazheniye, and (d) Busan, also marked in (a). Recorded data is shown by a black curve. Simulation results at these locations from various scenarios in are shown in different colors: vertical deformation only (red), vertical and horizontal deformation (blue), vertical deformation and Rayleigh wave (orange), and all three (gray). Rupture origin time is marked with black arrows. Top panels show correlation coefficients of each simulated time series with the recorded data in 30-min intervals.

Murotani *et al* [2015] and Kim *et al* [2019] both concluded that bathymetry plays a significant role in the higher frequency content of back-arc tsunamis. This effect is more noticeable in the presence of smaller deformation, e.g., in the case of Busan where the 2011 tsunami arrived more than one hour later than the Russian sites (Figs. 11b–d). Ray-tracing experiments confirm that the Japanese sites as well as Busan experience considerably more complex wavefronts than those on the far side of the Sea of Japan, due to the entrapment of tsunami energetics in the complex southern bathymetry (section S8 in supplementary material). Our results show that the contribution of Rayleigh waves to the 2011 Tohoku back-arc tsunami at locations in the intermediate-field may be important, as their addition slightly improves fits to the observed signal (~30% increase in CC) at higher frequencies (during the first few minutes of the records after origin time) in Rudnaya Pristan but not in Preobrazheniye (Fig. 11b). While these stations are approximately in the same radiation Rayleigh lobes, it seems that the interaction of surface waves with bathymetry complicates their contribution as is the case with Preobrazheniye. This probably led to the higher frequency content of the signal in Rudnaya Pristan tide gauge data (see section 9 in supplementary material). In fact, by dividing the back-arc deformation into near- and far-field components (near Japan and Russia, respectively) we can show that the high-frequency part of the record at Rudnaya Pristan can be better reproduced by considering only the far-field component, while the near-field deformation which is farther from the recording station provides a better match of amplitudes as well as the longer-periods in the data (supplementary material).

5. Potential Back-arc Tsunami Hazard in the Sea of Japan

We use the proposed rupture locations and geometries from previous studies as potential future sources that are large enough to produce back-arc tsunamis in the Sea of Japan. Here, we do not include surface waves in the simulations as our results from section 4 showed their contribution may be significant only in the presence of simple bathymetry, i.e., the shallow northwestern (Russian) side of the Sea of Japan where the tsunami will be attenuated faster. Our choice is also based on the fact that we are mainly investigating the largest amplitudes, not the first, high frequency portion of tsunamis in order to provide estimates of the back-arc hazard. Also, for the hypothetical and speculative scenarios in sections 5.1 and 5.2, inclusion of the unconstrained surface waves without observational basis is likely to result in systematic accumulation of errors and unrealistic tsunami amplitudes.

5.1 Japan Trench

A successive cascade of ruptures on the fault patches at the Japan Trench can occur during a single large megathrust [e.g., Satake, 2015], similar to the 2011 Tohoku event [Stein & Okal, 2011; Noda & Lapusta, 2013]. As a given paleoseismic window may not capture long-term trends in seismicity [Salditch *et al*, 2020], such large rupture areas can be keys to understanding the maximum possible earthquake and tsunami hazards.

We construct a composite rupture area by joining the previous M_S 7.1-7.8 events in 1936, 1937, 1938 and 1978 in the Miyagi-oki sequence, spanning a total geographic area of ~300 km × ~150 km (Abe, 1977; Umino et al, 2006; Satake, 2015), i.e., roughly 50% of the 2011

mainshock rupture area. We replace the 1936 event with its colocated 2005 counterpart because of better data as shown in Fig. 12 (also see Table S2 in supplementary material). Using earthquake scaling laws [Geller, 1976] for a constant stress drop and assuming a uniform convergence rate along the trench, we first compute a field of static deformation for a source (model I) with the same seismic moment and mechanism as the 2011 Tohoku located at an average epicenter of the sequence (Fig. 13.Ia). We then design a second scenario (model II) as a source similar to model I, but with a smaller magnitude (M_w=8.8) scaled down from the 2011 Tohoku mechanism (Fig. 13.IIa). As a third scenario (model III), we make a composite mechanism by superimposing the 1936-1978 sequence and assigning a scaled down moment (M_w=8.8) to match the rupture area (Fig. 13.IIIa). This mechanism has a Kagan aperture [Kagan, 1991] of ~23º from the 2011 Tohoku. Lastly, we design a fourth scenario (model IV) with the same mechanism as model III, but with a moment equal to that of 2011 Tohoku. We then simulate the back-arc tsunamis from these sources using the same hydrodynamic conditions from section 4.3. These simulations show that while the back-arc propagation patterns of the composite sources are fairly similar (CC=0.55), the maximum tsunami amplitudes from the large source are twice as large as the smaller event. Also, back-arc tsunami amplitudes close to ~1 m are expected near Niigata at the coast of Japan, similar to the 2011 event (see Fig. 13).

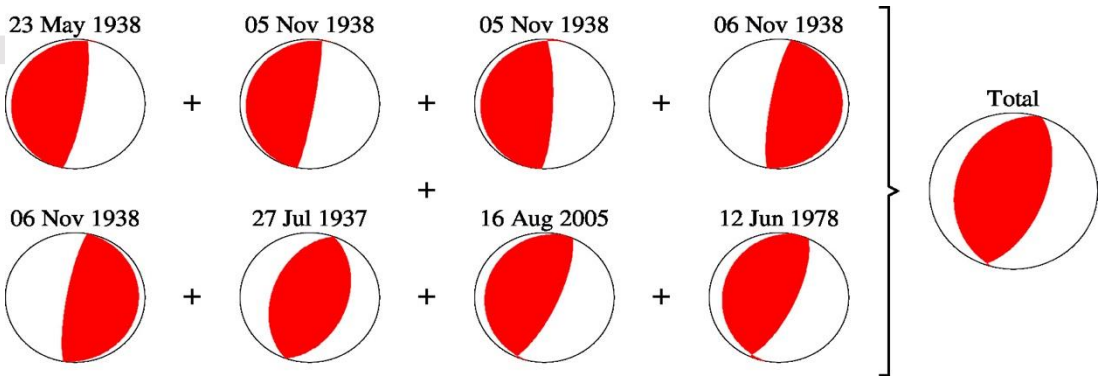

Figure 12. The Miyagi-oki sequence used to create the composite source along the Japan Trench. See Table S2 for details of focal mechanisms.

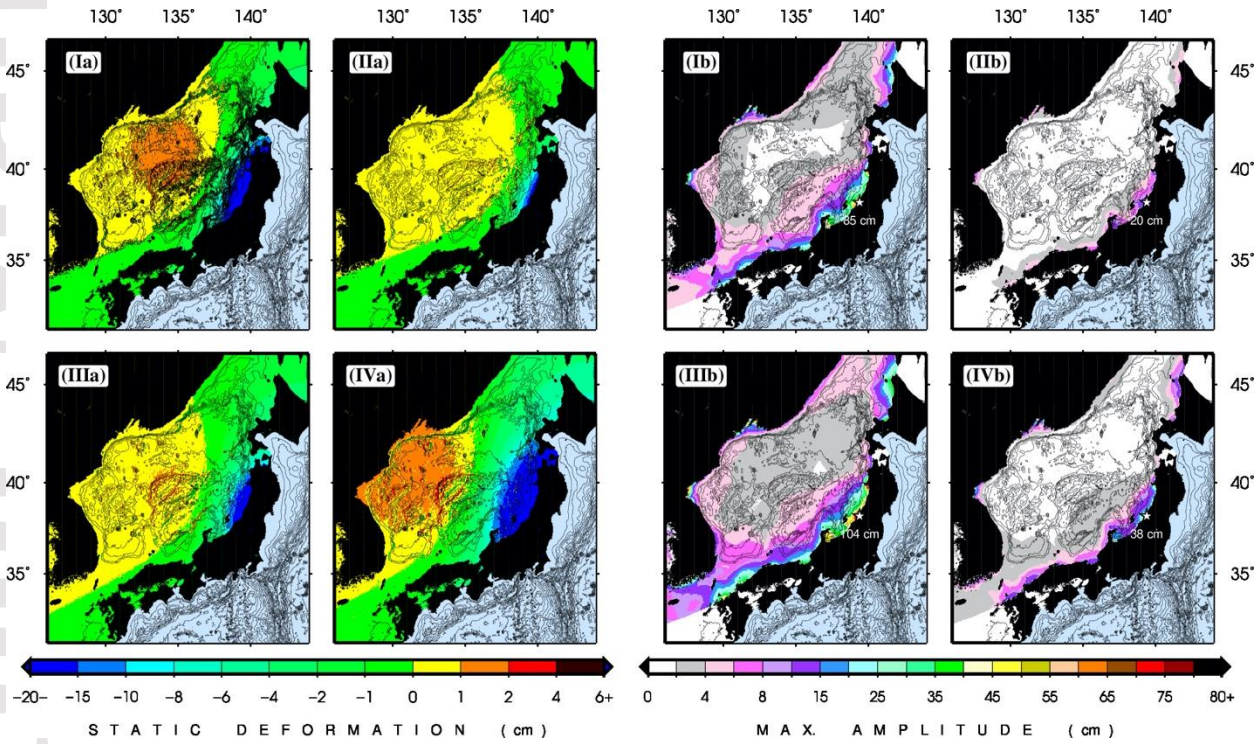

Figure 13. Sea floor deformation calculated for sources **(Ia)** identical to 2011 Tohoku but at the average epicenter of the 1936-1978 sequence, **(IIa)** with the same geometry as 2011 Tohoku at this location, but with smaller moment to match the smaller rupture area (M_w=8.8), **(IIIa)** with a composite mechanism from the 1936-1978 sequence and a moment scaled down to rupture area, and **(IVa)** same as (IIIa) with a moment increased to that of the 2011 Tohoku. **(Ib)-(IVb)** Maximum tsunami amplitudes from simulation of (Ia) to (IVa) scenarios. The fore-arc area is masked to focus on the back-arc tsunami.

5.2 Nankai Trough

While M>8 earthquakes have been frequently documented in the Nankai Trough [Ishibashi, 2004], M~9 events are also deemed possible through joining all the segments in single large ruptures [Yokota *et al*, 2016]. Using the same simulation conditions as in sections 4.1.3 and 5.1, we simulate back-arc tsunamis in the Sea of Japan for four rupture scenarios from combinations of the blocks proposed by Furumura *et al* [2011] as shown in Figs. 14.Ia to 14.IVa. Various permutations in the used blocks result in sources with M_w=8.6 (model I) and M_w=8.8 (models II to IV) (see section S11 in supplementary material for more details). Simulation results for these scenarios are shown in Figs. 14.Ib and 14.IVb (note the different color palettes used in Figs. 13 and 14). These simulations suggest that earthquakes in the Nankai Trough would generate very small tsunamis in the Sea of Japan, barely reaching 10 cm. This is mainly due to a very wide (>400 km) continental arc and shallow continental shelf in the back-arc region. While the ruptures in these scenarios are closer to Busan compared to those in the Japan Trench (section 5.1), the back-arc arrivals at Busan are negligible. This is probably due to the very shallow back-arc basin in the Korea Strait (<150 m deep) which results in significant attenuation. Similarly, the trapped edge waves on the shallow continental shelf from the fore-arc tsunami may not be notable at Busan due to their long paths in very shallow waters.

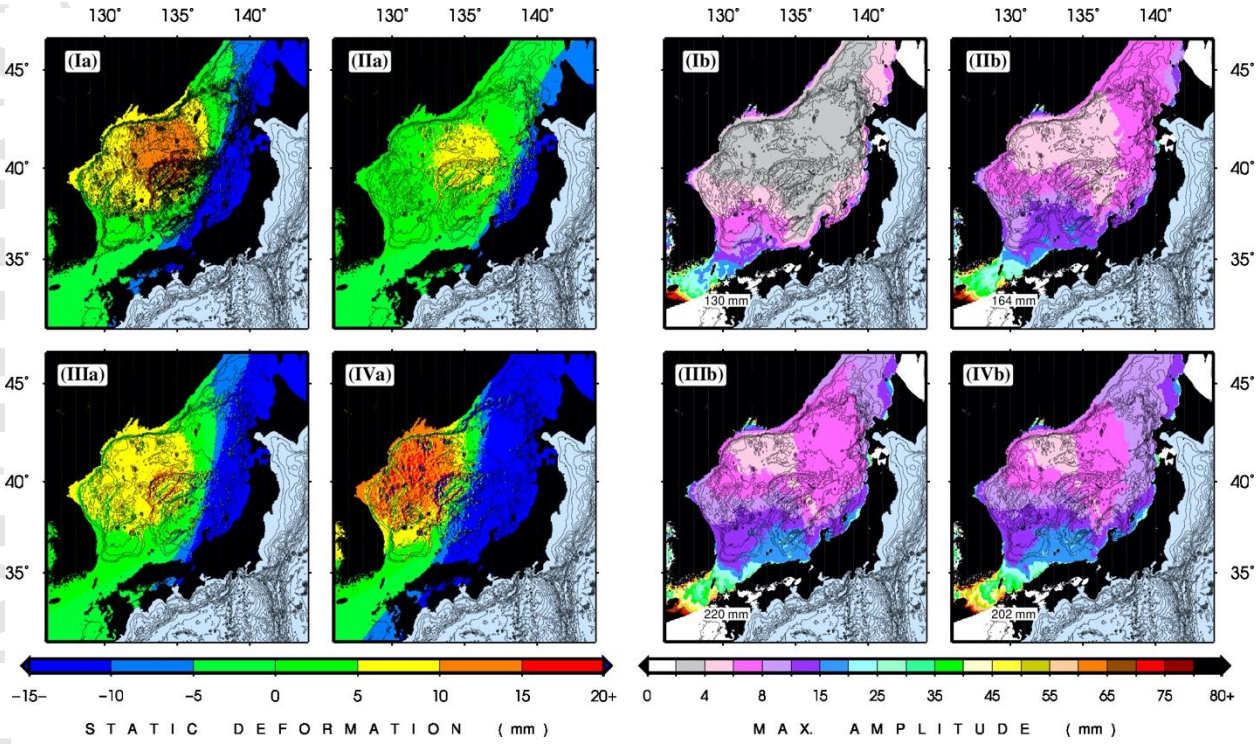

Figure 14. (Ia)-(IVa) Sea floor deformation fields from the four source scenarios in the Nankai Trough. **(Ib)-(IVb)** Fields of maximum amplitudes from the sources in (Ia) to (IVa).

6. Discussion and Conclusion

We present a simple dislocation model as the source of back-arc tsunamis explaining various features of these events (Figs. 2 & 7). Our results show that the most important source parameter affecting back-arc tsunamis is seismic moment which controls rupture dimensions, especially the down-dip extent of dislocation. We find that among the geometrical source parameters, the energy of back-arc tsunamis is only affected by dip angle (δ in Figs. 2 & 7). In this regard, our simulation of synthetic scenarios in flat oceans show that back-arc tsunami energetics (as a measure of tsunami frequency or wavenumber; e.g., Okal [2021]) are inversely proportional to dip of rupture plane. This is due to the effect of dip on the dominant frequency of back-arc tsunamis. We attribute this to the influence of dip angle on the surface expression of rupture, or the effective fault width. In our dipping plane model, a shallower dip of fault plane would result in a wider *area* of surface deformation (i.e., a larger length scale) and hence increasing the dominant period of the excited tsunami. Conversely, we report a rise in maximum back-arc tsunami amplitudes as a result of increasing dip angle for large megathrusts (Fig. 6). This is due to the larger *size* of deformation at higher dip angle as expected from theory of elastic deformation.

Fault width can be routinely approximated from focal geometry and seismic moment using earthquake scaling laws. We note that, finite rupture models are often confined to the tectonic fore-arc regions (e.g., Fig. 15 for the 2011 Tohoku-Oki earthquake), and the lower edge of the rupture remains somewhat speculative (see section S1 in the supplementary material). This is due to the fact that the extent of back-arc deformation for megathrust ruptures (the hatched areas in Figs. 15b and 15d) is mainly possible by down-dip extrapolation of slip distribution. One

must note that valid estimates of the down-dip extent of deformation are usually derived from physical models [e.g., Scholz, 1982]. This lack of constraint in the back-arc prevents the use of finite fault models in studying back-arc tsunamis. While the mentioned extrapolation result may provide some insight regarding the order of magnitude of back-arc tsunamis in the near- and far-field, it does not lead to meaningful details about propagation and frequency content of the waveforms (see the block analysis in section S12 in the supplementary material). We also note the importance of understanding the extent of back-arc deformation as it can lead to a more complete picture of the coseismic rupture [e.g., Shen *et al*, 2005]. Such models provide valuable alternatives to the otherwise non-unique values obtained from various methods (e.g., as manifested in the various solutions for the 2011 Tohoku rupture in the SRCMOD database [Mai & Thingbaijam, 2014]; also see the supplementary material).

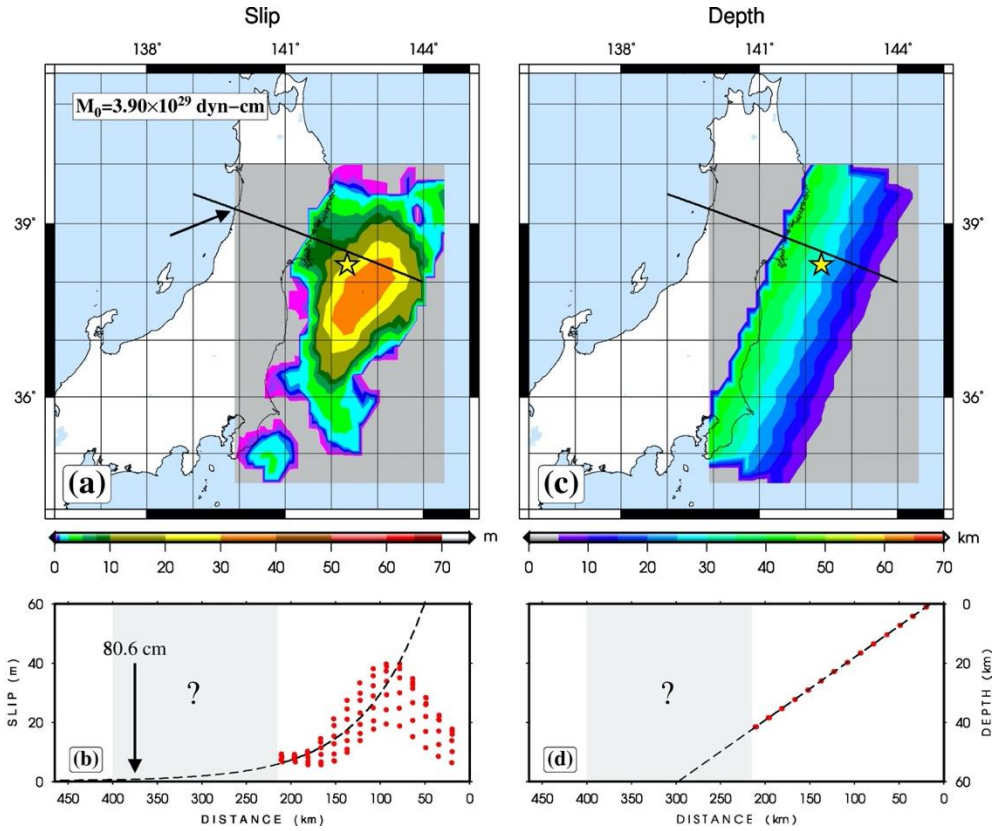

Figure 15. (a) Slip distribution of the 2011 Japan rupture from the finite fault solution by Ammon *et al* (2011); yellow star shows the rupture centroid. **(b)** Cross section of the slip model along the solid black line in (a); the dashed curve is an exponential fit to the slip values. The solid arrow shows the location of western Japanese shoreline also marked in (a) and the extrapolated slip from the fit. **(c)** Depth model used in the model in (a). **(d)** Cross section of the depth model along the solid black line in (a) and (c); the dashed line is a linear fit to the depth values. The hatched areas in (c) and (d) denoted by question mark show the region not covered by the source model [data from SRCMOD; Mai and Thingbaijam, 2014].

We find that ruptures with larger dip angles create larger and more widespread tsunamis in the back-arc, as shown quantitively via the metric MT as well as in Fig. 4. Thus, large megathrust earthquakes ($M_w \geqslant 9.0$) with intermediate dip angles (~20^o) are expected to create larger, more hazardous tsunamis in back-arc basins. Based on this model, the effective width calculated as the extent of back-arc depression in a direction perpendicular to the trench

determines the main properties of back-arc tsunamis (Figs. 7 and 8). While larger ruptures result in slip fields closer to surface (i.e., producing more significant surface deformation), the focal depth of such events does not seem to have a significant impact (Figs. 7, 8 and 9).

Our simulations of back-arc tsunamis for the Sea of Japan form the 2011 Tohoku rupture confirm Murotani *et al*'s [2015] conclusion on the significant contribution of horizontal deformation and the effect of complex bathymetry. In addition, we find that the contribution of Rayleigh waves to back-arc tsunami amplitudes, especially in the case of small static deformations, must be considered at regions with simple bathymetry (e.g., sites such as Rudnaya Pristan at the northwestern margin of the Sea of Japan). In locations at or near deformation nodes, addition of surface waves would potentially improve the quality of simulations, especially at higher (although low-amplitude) frequencies. This is best demonstrated in the case of Busan and Okushiri which were located at a deformation node of the 2011 Tohoku event.

Numerical simulations of the back-arc tsunamis from sources at and around the Japan Trench reveal the potential of back-arc tsunamis with coastal amplitudes reaching more than 1 m in western Japan and up to ~50 cm on the far side of the Sea of Japan (Fig. 13). While such amplitudes are very small compared to the fore-arc run-up values (i.e., >20 m close to the epicenter) and often ignored in the wake of fore-arc catastrophes, they must be taken seriously in a basin which is otherwise deemed as safe from tsunamis. We emphasize that the reported coastal amplitudes from the simulations in this study are at a distance from the coastlines and are thus smaller than run-up [Synolakis, 1991]. In other words, the on-land tsunami amplitudes will be relatively larger than our calculations while following similar along-coast patterns. As predicted by our dislocation model, our simulation of potential sources near Honshu with a larger

dip angle compared to 2011 Tohoku leads to a larger back-arc tsunami (also see section S10 in supplementary material).

Simulation of tsunamis from potential sources in the Nankai Trough reveal that these ruptures will not create significant tsunami hazard (with amplitudes smaller than 10 cm) in the Sea of Japan. We attribute this deficiency in back-arc tsunami amplitudes (compared to the cases in Japan Trench) to the wider continental arc as well as a large, shallow continental shelf in the southern back-arc. Similar to the case of ruptures in Japan Trench, small coseismic amplitudes in Korea are due to the close proximity to deformation nodes.

While our simple model does not consider non-uniform slip which can result in uncertainties in resolving definitive rupture dimensions, we note that such deficiencies (e.g., in depth, dip angle, and seismic moment) are inherent to seismic, acoustic, and hydrodynamic analyses of the source (e.g., see section 2.1). Also, some regions such as Java seem to be immune to the back-arc tsunami hazard due to the large trench-to-coast distance (an average of ~450 km) and thus will stand out as outliers in our model. Similarly, our model is not sufficient for small or very large ruptures, i.e., M8 and M≥9.5 (although we note that the former is too small to excite notable back-arc tsunamis and the latter is extremely rare) and thus serves as first step in understanding back-arc tsunamis. It is important to note that the mismatch between predicted and simulated results is due to the under- and over-sampling of small (M8.5) and large (M9.5) sources.

Nevertheless, our model provides valuable constraints to the source in conjunction with other methods; the addition of any proxies on the down-dip extent of large megathrust ruptures is important in improving the otherwise obscured aspect of source dimensions. Our model can be readily used for M9 events in subduction zones with back-arc basins around the world as our

results show the possibility of relatively large tsunami amplitudes in the back-arc. Based on our results, tsunami hazard needs to be assessed and mitigated in various back-arc regions including Alaska-Aleutians, Peru-Chile, the Philippines, Sumatra (see section S13 in supplementary material) and Oaxaca in Mexico [e.g., Salaree *et al*, 2020]. This issue is especially important in the back-arc of Oaxaca, i.e., the Gulf of Mexico where highly populated regions and important economic facilities such as oil structures are exposed to high risk due to a very narrow continental arc (~200 km) and possibility of large megathrusts. While some limitations will arise from subduction zones with wider continental shelfs and back-arc basins, our model can yet prove useful by making adjustments to initial seismic parameters [Salaree *et al*, 2020].

Acknowledgement

The authors are grateful to Satoko Murotani for sharing tide gauge data from the Japanese stations, and for providing accounts of the 2011 Tohoku back-arc tsunami. We also thank Emile Okal for discussions on synthesis of surface waves. The bathymetry data used in this study is publicly available via GEBCO [GEBCO, 2021]. The tsunami simulation code is maintained and distributed by NOAA. Tide gauge data is available through the Sea Level Station Monitoring Facility (http://www.ioc-sealevelmonitoring.org/map.php) and Geospatial Information Authority of Japan (GSI) (https://www.gsi.go.jp/kanshi/tide_furnish.html). Several figures were created using Generic Mapping Tools [Wessel & Smith, 1998]. This study was funded by National Science Foundation grant PREEVENTS geosciences directorate No. 1663769.

Data Availability Statement:

The bathymetry data used in this study is publicly available via GEBCO [GEBCO, 2021]. The tsunami simulation code is maintained and distributed by NOAA (https://nctr.pmel.noaa.gov/nthmp/). Tide gauge data is available at the Flanders Marine Institute (VLIZ) [2022] via the Intergovernmental Oceanographic Commission (IOC) Sea Level Station Monitoring Facility (http://www.ioc-sealevelmonitoring.org/map.php) and Geospatial Information Authority of Japan (GSI) (https://www.gsi.go.jp/kanshi/tide_furnish.html). The finite rupture data were acquired from SRCMOD [Mai and Thingbaijam, 2014] available at http://equake-rc.info/srcmod.

Competing Interests Statement

The authors declare that they do not have any competing interests.

References

- Abe, K., 1977. Tectonic implications of the large Shioya-Oki earthquakes of 1938. *Tectonophysics*, **41**(4), pp.269-289.
- Abe, K., 2006. Dominant periods of the 2004 Sumatra tsunami and the estimated source size. *Earth, Planets and Space*, **58**(2), pp.217-221.
- Ammon, C.J., Lay, T., Kanamori, H. and Cleveland, M., 2011. A rupture model of the 2011 off the Pacific coast of Tohoku Earthquake. *Earth, Planets and Space*, **63**(7), pp.693-696.
- Ando, M., 1975. Source mechanisms and tectonic significance of historical earthquakes along the Nankai Trough, Japan. *Tectonophysics*, **27**(2), pp.119-140.

- Aranguiz, R., Catalán, P.A., Cecioni, C., Bellotti, G., Henriquez, P. and González, J., 2019. Tsunami resonance and spatial pattern of natural oscillation modes with multiple resonators. *Journal of Geophysical Research: Oceans*, **124**(11), pp.7797-7816.

- Barberopoulou, A., Qamar, A., Pratt, T.L., Creager, K.C. and Steele, W.P., 2004. Local amplification of seismic waves from the Denali Earthquake and damaging seiches in Lake Union, Seattle, Washington. *Geophysical Research Letters*, **31**(L03607), 5 pp.

- Berkhoff, J.C.W., 1976. Mathematical models for simple harmonic linear water waves: wave diffraction and refraction. *PhD. Dissertation*, 123p.

- Bilek, S.L. and Lay, T., 2018. Subduction zone megathrust earthquakes. Geosphere, 14(4), pp.1468-1500.

- Chlieh, M., Avouac, J.P., Hjorleifsdottir, V., Song, T.R.A., Ji, C., Sieh, K., Sladen, A., Hebert, H., Prawirodirdjo, L., Bock, Y. and Galetzka, J., 2007. Coseismic slip and afterslip of the great M_w 9.15 Sumatra–Andaman earthquake of 2004. *Bulletin of the Seismological Society of America*, 97(1A), pp.S152-S173.

- Duputel, Z., Rivera, L., Fukahata, Y. and Kanamori, H., 2012. Uncertainty estimations for seismic source inversions. *Geophysical Journal International*, **190**(2), pp.1243-1256.

- Dziewonski, A.M., Chou, T.A. and Woodhouse, J.H., 1981. Determination of earthquake source parameters from waveform data for studies of global and regional seismicity. *Journal of Geophysical Research: Solid Earth*, **86**(B4), pp.2825-2852.

- Ekström, G., Nettles, M. and Dziewonski, A.M., 2012. The global CMT project 2004–2010: Centroid-moment tensors for 13,017 earthquakes. *Physics of the Earth and Planetary Interiors*, **200**, pp.1-9.

- Fujiwara, T., Kodaira, S., No, T., Kaiho, Y., Takahashi, N. and Kaneda, Y., 2011. The 2011 Tohoku-Oki earthquake: Displacement reaching the trench axis. *Science*, **334**(6060), pp.1240-1240.

- Furumura, T., Imai, K. and Maeda, T., 2011. A revised tsunami source model for the 1707 Hoei earthquake and simulation of tsunami inundation of Ryujin Lake, Kyushu, Japan. *J Geophys Res: Solid Earth*, **116**(B2), 17p.

- Flanders Marine Institute (VLIZ), 2022, Intergovernmental Oceanographic Commission (IOC): Sea level station monitoring facility. Accessed at http://www.ioc-sealevelmonitoring.org on 2022-05-24 at VLIZ. DOI: 10.14284/482

- GEBCO, 2021. GEBCO Compilation Group: GEBCO 2021 Grid, (doi:10.5285/c6612cbe-50b3-0cff-e053-6c86abc09f8f).

- Geller, R.J., 1976. Scaling relations for earthquake source parameters and magnitudes. *Bulletin of the Seismological Society of America*, **66**(5), pp.1501-1523.

- Gica, E., Teng, M.H., Liu, P.L.F., Titov, V. and Zhou, H., 2007. Sensitivity analysis of source parameters for earthquake-generated distant tsunamis. *Journal of Waterway, Port, Coastal, and Ocean Engineering*, **133**(6), pp.429-441.

- Grapenthin, R. and Freymueller, J.T., 2011. The dynamics of a seismic wave field: Animation and analysis of kinematic GPS data recorded during the 2011 Tohoku-oki earthquake, Japan. *Geophysical Research Letters*, **38**(18).

- Grue, J., Pelinovsky, E.N., Fructus, D., Talipova, T. and Kharif, C., 2008. Formation of undular bores and solitary waves in the Strait of Malacca caused by the 26 December 2004 Indian Ocean tsunami. *Journal of Geophysical Research: Oceans*, **113**(C5).

- Hartzell, S.H. and Heaton, T.H., 1983. Inversion of strong ground motion and teleseismic waveform data for the fault rupture history of the 1979 Imperial Valley, California, earthquake. *Bulletin of the Seismological Society of America*, **73**(6A), pp.1553-1583.

- Hashimoto, C., Noda, A., Sagiya, T. and Matsu'ura, M., 2009. Interplate seismogenic zones along the Kuril–Japan trench inferred from GPS data inversion. Nature Geoscience, 2(2), pp.141-144.

- Heidarzadeh, M. and Satake, K., 2013. Waveform and spectral analyses of the 2011 Japan tsunami records on tide gauge and DART stations across the Pacific Ocean. *Pure and Applied Geophysics*, **170**(6), pp.1275-1293.

- Ide, S., Baltay, A. and Beroza, G.C., 2011. Shallow dynamic overshoot and energetic deep rupture in the 2011 Mw 9.0 Tohoku-Oki earthquake. *Science*, **332**(6036), pp.1426-1429.

- Ishibashi, K., 2004. Status of historical seismology in Japan. *Annals of Geophysics*, **47**(2-3), pp. 338-369

- Ito, T., Ozawa, K., Watanabe, T. and Sagiya, T., 2011b. Slip distribution of the 2011 off the Pacific coast of Tohoku earthquake inferred from geodetic data. *Earth, Planets and Space*, **63**(7), pp.627-630.

- Ito, T., T., Osada, Y., Kido, M., Inazu, D., Hayashi, Y., Tsushima, H., Hino, R. and Fujimoto, H., 2011a. Frontal wedge deformation near the source region of the 2011 Tohoku-Oki earthquake. *Geophysical Research Letters*, **38**(7).

- Kagan, Y.Y., 1991. 3-D rotation of double-couple earthquake sources. *Geophysical Journal International*, **106**(3), pp.709-716.

- Kanamori, H., Rivera, L. and Lambotte, S., 2019. Evidence for a large strike-slip component during the 1960 Chilean earthquake. *Geophys J Int*, **218**(1), pp.1-32.

- Kido, M., Osada, Y., Fujimoto, H., Hino, R. and Ito, Y., 2011. Trench-normal variation in observed seafloor displacements associated with the 2011 Tohoku-Oki earthquake. *Geophysical Research Letters*, **38**(24).

- Kim, S., Kang, T.S., Rhie, J. and Baag, S.Y., 2019. Validating slip distribution models of the 2011 Tohoku earthquake with diffracted tsunami and uplift-induced sea waves in the backarc region. *Geophysical Journal International*, **216**(3), pp.1578-1593.

- Kundu, P.K., Cohen, I.M. and Dowling, D.R., 2015. Fluid mechanics. *Academic Press*, 928p.

- Noda, H. and Lapusta, N., 2013. Stable creeping fault segments can become destructive as a result of dynamic weakening. *Nature*, **493**(7433), pp.518-521.

- Lay, T., Kanamori, H., Ammon, C.J., Nettles, M., Ward, S.N., Aster, R.C., Beck, S.L., Bilek, S.L., Brudzinski, M.R., Butler, R. and DeShon, H.R., 2005. The great Sumatra-Andaman earthquake of 26 December 2004. *Science*, **308**(5725), pp.1127-1133.

- Lay, T., Ammon, C.J., Kanamori, H., Koper, K.D., Sufri, O. and Hutko, A.R., 2010. Teleseismic inversion for rupture process of the 27 February 2010 Chile (Mw 8.8) earthquake. *Geophysical Research Letters*, **37**(13).

- Lay, T., 2018. A review of the rupture characteristics of the 2011 Tohoku-oki Mw 9.1 earthquake. *Tectonophysics*, **733**, pp.4-36.

- Lee, J.W., Park, E.H., Park, S.C., Lee, D.K. and Lee, J.H., 2016. Numerical Simulations of the 2011 Tohoku, Japan Tsunami Forerunner Observed in Korea using the Bathymetry Effect. *Journal of Korean Society of Coastal and Ocean Engineers*, **28**(5), pp.265-276.

- Mai, P.M. and Thingbaijam, K.K.S., 2014. SRCMOD: An online database of finite-fault rupture models. *Seismological Research Letters*, **85**(6), pp.1348-1357.

- Mansinha, L.A. and Smylie, D.E., 1971. The displacement fields of inclined faults. *Bulletin of the Seismological Society of America*, **61**(5), pp.1433-1440.

- Meng, L., Inbal, A. and Ampuero, J.P., 2011. A window into the complexity of the dynamic rupture of the 2011 Mw 9 Tohoku-Oki earthquake. *Geophysical Research Letters*, **38**(7).

- Mori, N., Takahashi, T., Yasuda, T. and Yanagisawa, H., 2011. Survey of 2011 Tohoku earthquake tsunami inundation and run-up. *Geophysical Research Letters*, **38**(7).

- Murotani, S., Iwai, M., Satake, K., Shevchenko, G. and Loskutov, A., 2015. Tsunami forerunner of the 2011 Tohoku Earthquake observed in the Sea of Japan. *Pure and Applied Geophysics*, **172**(3-4), pp.683-697.

- Okada, Y., 1985. Surface deformation due to shear and tensile faults in a half-space. Bulletin of the Seismological Society of America, 75(4), pp.1135-1154.

- Okal, E.A., 2021. The energy of a tsunami generated by dynamic uplift of the ocean bottom. I. Analytical solutions. *Pure and Applied Geophysics*, pp.1-15.

- Okal, E.A. and Synolakis, C.E., 2004. Source discriminants for near-field tsunamis. *Geophysical Journal International*, **158**(3), pp.899-912.

- Plafker, G., 1997. Catastrophic tsunami generated by submarine slides and backarc thrusting during the 1992 earthquake on eastern Flores I., Indonesia, *Geol. Soc. Am. Cordill. Sect.*, **29**, 57 (abstract with programme).

- Pollitz, F.F., 1996. Coseismic deformation from earthquake faulting on a layered spherical Earth. *Geophysical Journal International*, **125**(1), pp.1-14.

- Pollitz, F.F., Bürgmann, R. and Banerjee, P., 2011. Geodetic slip model of the 2011 M9.0 Tohoku earthquake. *Geophysical Research Letters*, **38**(7).

- Rabinovich, A.B., 1997. Spectral analysis of tsunami waves: Separation of source and topography effects. *Journal of Geophysical Research: Oceans*, **102**(C6), pp.12663-12676.

- Saito, T., Baba, T., Inazu, D., Takemura, S. and Fukuyama, E., 2019. Synthesizing sea surface height change including seismic waves and tsunami using a dynamic rupture scenario of anticipated Nankai trough earthquakes. *Tectonophysics*, **769**, p.228166.

- Salaree, A., Saloor, N. and Huang, Y., 2020, December. Back-arc tsunami hazard in the Gulf of Mexico from Oaxaca earthquakes: Lessons from past events. **in:** *AGU Fall Meeting Abstracts* (Vol. **2020**, pp. NH017-07).

- Salaree, A. and Okal, E.A., 2015. Field survey and modelling of the Caspian Sea tsunami of 1990 June 20. *Geophys J Int*, **201**(2), pp.621-639.

- Salaree, A. and Okal, E.A., 2020. Effects of bathymetry complexity on tsunami propagation: A spherical harmonics approach. *Geophysical Journal International*, **223**(1), pp.632-647.

- Salaree, A., Huang, Y., Ramos, M.D. and Stein, S., 2021. Relative tsunami hazard from segments of Cascadia subduction zone for Mw 7.5–9.2 earthquakes. *Geophysical Research Letters*, **48**(16), p.e2021GL094174.

- Salditch, L., Stein, S., Neely, J., Spencer, B.D., Brooks, E.M., Agnon, A. and Liu, M., 2020. Earthquake supercycles and Long-Term Fault Memory. *Tectonophysics*, **774**, p.228289.

- Satake, K., 2015. Geological and historical evidence of irregular recurrent earthquakes in Japan. *Philosophical Transactions of the Royal Society A: Mathematical, Physical and Engineering Sciences*, **373**(2053), p.20140375.

- Satake, K., Ishibe, T., Murotani, S., Mulia, I.E. and Gusman, A.R., 2022. Effects of uncertainty in fault parameters on deterministic tsunami hazard assessment: examples for

active faults along the eastern margin of the Sea of Japan. *Earth, Planets and Space*, **74**(1), pp.1-20.

- Sato, M., Ishikawa, T., Ujihara, N., Yoshida, S., Fujita, M., Mochizuki, M. and Asada, A., 2011. Displacement above the hypocenter of the 2011 Tohoku-Oki earthquake. *Science*, **332**(6036), pp.1395-1395.

- Shao, G., Li, X., Ji, C. and Maeda, T., 2011. Focal mechanism and slip history of the 2011 M w 9.1 off the Pacific coast of Tohoku Earthquake, constrained with teleseismic body and surface waves. *Earth, Planets and Space*, **63**(7), pp.559-564.

- Scholz, C.H., 1982. Scaling laws for large earthquakes: consequences for physical models. *Bulletin of the Seismological Society of America*, **72**(1), pp.1-14.

- Shen, Z.K., Lü, J., Wang, M. and Bürgmann, R., 2005. Contemporary crustal deformation around the southeast borderland of the Tibetan Plateau. *Journal of Geophysical Research: Solid Earth*, **110**(B11).

- Shevchenko, G., Ivelskaya, T. and Loskutov, A., 2014. Characteristics of the 2011 Great Tohoku tsunami on the Russian Far East coast: Deep-water and coastal observations. *Pure and Applied Geophysics*, **171**(12), pp.3329-3350.

- Shimozono, T., Sato, S., Okayasu, A., Tajima, Y., Fritz, H.M., Liu, H. and Takagawa, T., 2012. Propagation and inundation characteristics of the 2011 Tohoku tsunami on the central Sanriku coast. *Coastal Engineering Journal*, **54**(01), p.1250004.

- Stein, S. and Okal, E.A., 2011. The size of the 2011 Tohoku earthquake need not have been a surprise. *Eos, Transactions American Geophysical Union*, **92**(27), pp.227-228.

- Synolakis, C.E., 1991. Green's law and the evolution of solitary waves. *Physics of Fluids A: Fluid Dynamics*, **3**(3), pp.490-491.

- Synolakis, C.E., Bernard, E.N., Titov, V.V., Kânoğlu, U.T.K.U. and Gonzalez, F.I., 2008. Validation and verification of tsunami numerical models. **In:** *Tsunami science four years after the 2004 indian ocean tsunami* (pp. 2197-2228). Birkhäuser Basel.

- Tang, L., Titov, V.V. and Chamberlin, C.D., 2009. Development, testing, and applications of site‐specific tsunami inundation models for real‐time forecasting. *J Geophys Res: Oceans*, **114**(C12).

- Tanioka, Y. and Satake, K., 1996. Tsunami generation by horizontal displacement of ocean bottom. *Geophysical Research Letters*, **23**(8), pp.861-864.

- Thingbaijam, K.K.S., Martin Mai, P. and Goda, K., 2017. New empirical earthquake source‐scaling laws. *Bulletin of the Seismological Society of America*, **107**(5), pp.2225-2246.

- Titov, V.V. and Gonzalez, F.I., 1997. Implementation and testing of the Method of Splitting Tsunami (MOST) model. *NOAA Technical Memorandum ERL PMEL-112*, Contribution No. 1927, 14p.

- Titov, V.V., Mofjeld, H.O., González, F.I. and Newman, J.C., 1999. Offshore forecasting of Hawaiian tsunamis generated in Alaskan-Aleutian subduction zone. *NOAA Technical Memorandum ERL PMEL*, **114**, 22p.

- Titov V, Kânoğlu U, Synolakis C (2016) Development of MOST for real-time tsunami forecasting. *J Waterway, Port, Coast Ocean Engineering*, **142**:03116004-1–03116004-16

- Titov, V.V. and Synolakis, C.E., 1995. Modeling of breaking and nonbreaking long-wave evolution and runup using VTCS-2. *Journal of Waterway, Port, Coastal, and Ocean Engineering*, **121**(6), pp.308-316.

- Titov, V.V. and Synolakis, C.E., 1998. Numerical modeling of tidal wave runup. *J. Waterway, Port, Coastal, and Ocean Engineering*, **124**(4), pp.157-171.

- Umino, N., Kono, T., Okada, T., Nakajima, J., Matsuzawa, T., Uchida, N., Hasegawa, A., Tamura, Y. and Aoki, G., 2006. Revisiting the three M-7 Miyagi-oki earthquakes in the 1930s: possible seismogenic slip on asperities that were re-ruptured during the 1978 M= 7.4 Miyagi-oki earthquake. *Earth, Planets and Space*, **58**(12), pp.1587-1592.

- Ward, S.N., 1980. Relationships of tsunami generation and an earthquake source. *Journal of Physics of the Earth*, **28**(5), pp.441-474.

- Weatherall, P., Marks, K.M., Jakobsson, M., Schmitt, T., Tani, S., Arndt, J.E., Rovere, M., Chayes, D., Ferrini, V. and Wigley, R., 2015. A new digital bathymetric model of the world's oceans. *Earth and Space Science*, **2**(8), pp.331-345.

-
- Wessel, P. and Smith, W.H., 1998. New, improved version of Generic Mapping Tools released. Eos, Transactions American Geophysical Union, 79(47), pp.579-579.
-
-
- Yanenko, N.N., 1971, The Method of Fractional Steps, Springer
-
- Yokota, Y., Ishikawa, T., Watanabe, S.I., Tashiro, T. and Asada, A., 2016. Seafloor geodetic constraints on interplate coupling of the Nankai Trough megathrust zone. *Nature*, **534**(7607), pp.374-377.

Supporting Information References

- Abe, K., 1977. Tectonic implications of the large Shioya-Oki earthquakes of 1938. *Tectonophysics*, **41**(4), pp.269-289.

- Furumura, T., Imai, K. and Maeda, T., 2011. A revised tsunami source model for the 1707 Hoei earthquake and simulation of tsunami inundation of Ryujin Lake, Kyushu, Japan. *Journal of Geophysical Research: Solid Earth*, **116**(B2).

- Gilbert, F. and Dziewonski, A.M., 1975. An application of normal mode theory to the retrieval of structural parameters and source mechanisms from seismic spectra. *Philosophical Transactions of the Royal Society of London*. **in:** Series A, Mathematical and Physical Sciences, 278(1280), pp.187-269.

- Kanamori, H. & Cipar, J. J., 1974. Focal process of the great Chilean earth- quake May 22, 1960, *Physics of the Earth and Planetary Interiors*, **9**(2), 128–136.

- Kanamori, H., 1970. Synthesis of the long-period surface waves and its application to earthquake source studies–Kurile Islands earthquake of October 13, 1963, *Journal of Geophysical Research*, **75**(26), 5011–5027.

- Kian, R., 2015. Tsunami induced wave and current amplification and sedimentation in closed basins (Doctoral dissertation, *Ph. D. Dissertation*, Middle East Technical University, Ankara, Turkey), 189 pp.

- Koketsu, K., Yokota, Y., Nishimura, N., Yagi, Y., Miyazaki, S.I., Satake, K., Fujii, Y., Miyake, H., Sakai, S.I., Yamanaka, Y. and Okada, T., 2011. A unified source model for the 2011 Tohoku earthquake. *Earth and Planetary Science Letters*, **310**(3-4), pp.480-487.

- Mai, P.M. and Thingbaijam, K.K.S., 2014. SRCMOD: An online database of finite-fault rupture models. *Seismological Research Letters*, **85**(6), pp.1348-1357.

- Okal, E.A., 1976. A surface-wave investigation of the rupture mechanism of the Gobi-Altai (December 4, 1957) earthquake. *Physics of the Earth and Planetary Interiors*, **12**(4), pp.319-328.

- Okal, E.A., 2017. The excitation of tsunamis by deep earthquakes. *Geophysical Journal International*, **209**(1), pp.234-249.

- Rost, S. and Thomas, C., 2002. Array seismology: Methods and applications. *Reviews of geophysics*, **40**(3), pp.2-1.

- Saito, M., 1967. Excitation of free oscillations and surface waves by a point source in a vertically heterogeneous earth. *Journal of Geophysical Research*, **72**(14), pp.3689-3699.

- Salaree, A. and Okal, E.A., 2020. Tsunami simulations along the Eastern African coast from mega-earthquake sources in the Indian Ocean. *Arabian Journal of Geosciences*, **13**(20), pp.1-13.

- Satake, K., 1988. Effects of bathymetry on tsunami propagation: Application of ray tracing to tsunamis. *Pure and Applied Geophysics*, **126**(1), pp.27-36.

- Seno, T., Shimazaki, K., Somerville, P., Sudo, K. and Eguchi, T., 1980. Rupture process of the Miyagi-Oki, Japan, earthquake of June 12, 1978. *Physics of the Earth and Planetary Interiors*, **23**(1), pp.39-61.

- Titov, V.V., Mofjeld, H.O., González, F.I. and Newman, J.C., 1999. Offshore forecasting of Hawaiian tsunamis generated in Alaskan-Aleutian subduction zone. *NOAA Technical Memorandum ERL PMEL*, **114**, p.22.

- Umino, N., Kono, T., Okada, T., Nakajima, J., Matsuzawa, T., Uchida, N., Hasegawa, A., Tamura, Y. and Aoki, G., 2006. Revisiting the three M-7 Miyagi-oki earthquakes in the 1930s: possible seismogenic slip on asperities that were re-ruptured during the 1978 M= 7.4 Miyagi-oki earthquake. *Earth, planets and space*, **58**(12), pp.1587-1592.

- Woods, M.T. and Okal, E.A., 1987. Effect of variable bathymetry on the amplitude of teleseismic tsunamis: A ray-tracing experiment. *Geophysical Research Letters*, **14**(7), pp.765-768.

Data Availability Statement:

The bathymetry data used in this study is publicly available via GEBCO [GEBCO, 2021]. The tsunami simulation code is maintained and distributed by NOAA (https://nctr.pmel.noaa.gov/nthmp/). Tide gauge data is available at the Flanders Marine Institute (VLIZ) [2022] via the Intergovernmental Oceanographic Commission (IOC) Sea Level Station Monitoring Facility (http://www.ioc-sealevelmonitoring.org/map.php) and Geospatial Information Authority of Japan (GSI) (https://www.gsi.go.jp/kanshi/tide_furnish.html). The finite rupture data were acquired from SRCMOD [Mai and Thingbaijam, 2014] available at http://equake-rc.info/srcmod.

Please add the following to the reference list:

- Bilek, S.L. and Lay, T., 2018. Subduction zone megathrust earthquakes. *Geosphere*, **14**(4), pp.1468-1500.
- Flanders Marine Institute (VLIZ), 2022, Intergovernmental Oceanographic Commission (IOC): Sea level station monitoring facility. Accessed at http://www.ioc-sealevelmonitoring.org on 2022-05-24 at VLIZ. DOI: 10.14284/482
- Wessel, P. and Smith, W.H., 1998. New, improved version of Generic Mapping Tools released. *Eos, Transactions American Geophysical Union*, **79**(47), pp.579-579.
- Yanenko, N.N., 1971, *The Method of Fractional Steps*, Springer

---

Please remove the following from the reference list:

- Aki, K., 1972. Earthquake mechanism. *Tectonophysics*, **13**(1-4), pp.423-446.
- Mavko, G.M., 1981. Mechanics of motion on major faults. *Annual Review of Earth and Planetary Sciences*, **9**(1), pp.81-111.
- Ben-Menahem, A. and Rosenman, M., 1972. Amplitude patterns of tsunami waves from
- Duan, P. and Huang, C., 2019. Application of normal Morlet wavelet transform method to the damped harmonic analysis: On the isolation of the seismic normal modes ($_0S_0$ and $_0S_5$) in time domain. *Physics of the Earth and Planetary Interiors*, **288**, pp.26-36.

The following citations belong in the reference list for the supplementary material. They were included at the end of the main text as a separate list, at the request of the editorial staff during the review process.

- Gilbert & Dziewonski, 1975
- Kanamori & Cipar, 1974
- Kian, 2015
- Koketsu *et al*, 2011
- Okal, 1976
- Okal, 2017
- Rost & Thomas, 2002
- Saito, 1967
- Satake, 1988
- Seno, 1980 (We cannot find the 'Seno *et al*, 1978 in the text as suggested in your message. You may, however, be referring to lines #1014-1016 where 1978 is actually a part of the title). Please replace the reference in Table S2, i.e., Seno (1980) with Seno *et al* (1980).
- Woods & Okal, 1987

Please make the following corrections to the text:

- L120: Sholz, 1982 → Scholz, 1982
- L138: Chlieh, 2007 → Chlieh *et al*, 2007
- L138: Pollitz, 2011 → Pollitz *et al*, 2011
- L384: Fujiwara, 2011 → Fujiwara *et al*, 2011
- L425: Fujiwara, 2011 → Fujiwara *et al*, 2011
- L458: Barberopoulou, 2004 → Barberopoulou *et al*, 2004
- L544: Umino, 2006 → Umino *et al*, 2006
- [suppl. material; Table S2]: Seno (1980) → Seno *et al* (1980)

Please note that the following actually have been cited in the text:

- Grue *et al* [2008] (cited on line #75; we cannot find 'Grue et al, 2004' as listed in your message)

  Grue, J., Pelinovsky, E.N., Fructus, D., Talipova, T. and Kharif, C., 2008. Formation of undular bores and solitary waves in the Strait of Malacca caused by the 26 December 2004 Indian Ocean tsunami. *Journal of Geophysical Research: Oceans*, **113**(C5).

- Salaree & Okal [2020] (cited on line #303)

  Salaree, A. and Okal, E.A., 2020. Effects of bathymetry complexity on tsunami propagation: A spherical harmonics approach. *Geophysical Journal International*, **223**(1), pp.632-647.

- Titov *et al* [1999] (cited on line #219 of the text)

  Titov, V.V., Mofjeld, H.O., González, F.I. and Newman, J.C., 1999. Offshore forecasting of Hawaiian tsunamis generated in Alaskan-Aleutian subduction zone. NOAA Technical Memorandum ERL PMEL, 114, 22p.

- Lay [2005]: We cannot find this citation in the text, as suggested in your message. However, there is a Lay *et al*, 2005 which does already exist in the referenc list (lines #814-816).

Please note that the following are already included in the reference list:

- Grue [2008]: please see above.

- Korea, Lee [2016]: Please note that Korea is not a part of the reference. Lee *et al* [2016] is the correct reference and is included in the reference list.

- Satake [2015]: Please note that this reference is already provided in the reference list (lines #883-885).

Satake, K., 2015. Geological and historical evidence of irregular recurrent earthquakes in Japan. *Philosophical Transactions of the Royal Society A: Mathematical, Physical and Engineering Sciences*, **373**(2053), p.20140375.

- Mai and Thingbaijam [2014]: This reference is already included in the text. Please see e.g., line #651.